

Lattice Boltzmann model for immiscible three-phase flows with phase changeGuang Yang, Hangyu Chen, and Moran Wang ^{*}*Department of Engineering Mechanics and ASP, Tsinghua University, Beijing 100084, China*

(Received 5 February 2025; accepted 23 May 2025; published 16 June 2025)

This work presents a lattice Boltzmann (LB) model for immiscible multiphase flow with phase change. By integrating the pseudopotential model with the color-gradient model, the current model is capable of capturing phase change spontaneously during the immiscible multiphase flows for the first time, with corrected interaction forces at interfaces. The proposed model is comprehensively verified via multiple benchmark cases and applied to investigate the phase change effects on immiscible multiphase flow and displacement in porous media. Our simulation results reveal mechanisms from the gas blockage effects at different capillary numbers and the compressibility effect during immiscible multiphase displacement with phase change in porous media. The pronounced disparity between models that incorporate phase change or not underscores the critical importance of considering phase transitions in immiscible multiphase flow systems.

DOI: [10.1103/prh3-xhcb](https://doi.org/10.1103/prh3-xhcb)**I. INTRODUCTION**

Immiscible multiphase flow often coexists with phase transitions, resulting in a rich and complex dynamic interplay [1–4]. For instance, in an immiscible two-phase flow composed of oil and water, the oil may undergo phase changes due to variations of environmental temperature and pressure, leading to the formation of oil-gas-water three-phase flow system [1,2]. Similarly, in carbon geological sequestration, the immiscible two-phase flow composed of water and carbon dioxide (CO₂) [3,4], as well as the two-phase flow in water contamination remediation [5] may exhibit the same flow phenomena. The intricate interplay of phases and fluid dynamics in immiscible multiphase flows, combined with phase changes, presents significant challenges for both theoretical and experimental investigation [6,7]. Therefore, it is crucial to develop numerical methods to study immiscible multiphase flow with phase change.

For direct numerical simulation of immiscible multiphase flow, there are several existing macroscopic methods, such as the volume of fluid method [6,8], the level-set method [8,9], and the phase field method [10,11]. However, most phase-change models based on macroscopic methods require predefined vaporization nucleus and explicit calculation of the mass transfer rate between the liquid and the vapor phases [6,8,9,12]. Hence, such models cannot automatically capture the transitions between two-phase and three-phase flows.

On the other hand, mesoscopic methods, such as the lattice Boltzmann method (LBM), have excelled at multiphase as well as phase change simulations [13–15]. Various LBM models have been proposed to simulate multiphase flow, generally classified into four categories the color-gradient model [16,17], the pseudopotential model [18,19],

the free-energy model [20], and the phase-field model [21,22]. Although all four types of models can simulate multiphase flow successfully, each has its own advantages and limitations [23,24]. For example, the free-energy model shows good performance on multicomponent multiphase problems such as three-phase liquid-liquid-gas coexistence (even more) and flow [25], and the model shows thermodynamic consistency without any tuning [26]. Although free-energy model is powerful in non-phase-change multiphase problem, there is no effective free-energy based model to achieve the description of liquid-liquid-gas system with phase change process in the one of the components. In the pseudopotential model, the interfacial tension and thickness cannot be adjusted independently [15,27], while the phase-field model suffers the mass conservation issue [28]. In comparison, the color-gradient model shows good performance in low-density-ratio cases and overcomes the above-mentioned limitations and is widely adopted to study multiphase dynamics at micro- and nanoscales [29–31]. Some researchers also extended the color-gradient model to simulate three-phase flow as well as multiphase-viscoelastic flow [32]. However, the color-gradient model is only a phenomenological modeling of immiscible multiphase flow and lacks a rigorous thermodynamic basis, making it unsuitable for simulating phase change [23,30,33].

With respect to phase change flow simulation, the pseudopotential model is extensively employed [15,34–38]. Zhang and Chen [39] first simulated the boiling process with the pseudopotential model. To improve the density ratio and thermal consistency of the original pseudopotential model, many researchers proposed different force schemes [35,40–42], successfully simulating the boiling curve of the pool boiling process [43,44]. Nevertheless, such phase-change models are single-component multiphase model which are based on the equation of state (EOS) of pure substance [15,18]. More recently, some researchers also proposed the multi-component multiphase model to study evaporation in porous

^{*}Contact author: mrwang@mail.tsinghua.edu.cn

media [36,37,45]. However, in their research the two components are miscible, resulting in a two-component two-phase system. Consequently, current phase change models cannot simulate the transition between two-phase and three-phase flows as the phase change occurs in immiscible multiphase flow. Meanwhile, the lack of flexibility in interfacial parameters further limits the application of the pseudopotential model in immiscible multiphase flow [27].

Therefore, although multiphase LBM models for immiscible multiphase flow and phase-change flow have been developed individually, current models are unable to simulate both phenomena simultaneously. Furthermore, different multiphase models are suited to different physical problems. To the best of our knowledge, previous LBM models for multiphase flow with other complexity are all based on a single type multiphase model [15,23,24,27,30], with few attempts to couple different models to enhance their capabilities for more complex flow scenarios.

In this work, we propose a multiphase LBM model for simulating immiscible multiphase flow with phase change. By coupling the color-gradient model with the pseudopotential model, our approach leverages the strengths of both: the color-gradient model's capability for simulating immiscible multiphase flow and the pseudopotential model's capability for simulating phase change flow. This integration enables our model to automatically capture phase-change phenomena within immiscible multiphase flow. In Sec. II, we introduce the basic color-gradient model and its coupling with the pseudopotential model. Several benchmarks are presented in Sec. III to verify our model. In Sec. IV, we apply the model to investigate the effects of phase change on immiscible multiphase displacement in porous media. Finally, conclusions are drawn in Sec. V.

II. NUMERICAL METHODS

A. Color-gradient model for immiscible multiphase flow

The color-gradient model proposed by Leclaire *et al.* [30,33,46] is selected as the foundational model, offering independently control over interfacial tension, interface thickness, density ratio, and fluid ratio, making it a powerful tool to investigate multiphase flow [32,47,48]. Similarly to other color-gradient models, the two immiscible fluids are denoted by two colored distribution functions, f_i^b and f_i^r (with b representing blue and r representing red), while the total distributions $f_i = f_i^b + f_i^r$ [17,30]. The evolution equation of the distribution function can be written as [23,30,46],

$$\begin{aligned} & f_i^k(\mathbf{x} + \mathbf{e}_i \delta t, t + \delta t) - f_i^k(\mathbf{x}, t) \\ &= \Omega_i^{3,k} [\Omega_i^1 + \Omega_i^2 + \bar{F}_i], \quad k = r, b, \end{aligned} \quad (1)$$

where superscript k denotes either fluid b or fluid r , while Ω_i^1 , Ω_i^2 , and $\Omega_i^{3,k}$ represents the collision operator responsible for viscous effect, interfacial tension, and phase separation, respectively. \bar{F}_i is the source term that relates to the exter-

nal body force. The macroscopic variables can be calculated via [49,50]

$$\rho_k = \sum_i f_i^k, \quad \rho_k \mathbf{u}_k = \sum_i f_i^k \mathbf{e}_i + \frac{\rho_k \mathbf{F}}{2}. \quad (2)$$

$$\rho = \sum_k \rho^k, \quad \rho \mathbf{u} = \sum_k \rho_k \mathbf{u}_k. \quad (3)$$

Following Leclaire *et al.* [30], the viscous collision operator in multiple-relaxation time (MRT) [51,52] form can be expressed as

$$\Omega^1 = -\mathbf{M}^{-1} \mathbf{S} \mathbf{M} (\mathbf{f} - \mathbf{f}^{\text{eq}}), \quad (4)$$

where \mathbf{M} is the transformation matrix to the moment space, \mathbf{f} and \mathbf{f}^{eq} are the vector form of the distribution function and its equilibrium state, and \mathbf{S} is a diagonal matrix composed of the relaxation parameters. For the D3Q19 lattice employed in this work [30,50,51],

$$\begin{aligned} \mathbf{S} = \text{diag}(S_\rho, S_e, S_\varepsilon, S_j, S_q, S_j, S_q, S_j, S_q, S_v, S_\pi, \\ S_v, S_\pi, S_v, S_v, S_v, S_m, S_m, S_m), \end{aligned} \quad (5)$$

where S_v is related to the viscosity via $\frac{1}{S_v} = \bar{\tau} = \frac{\bar{\nu}}{c_s^2 \delta t} + \frac{1}{2}$, $\bar{\nu}$ denotes the harmonic density weighted average viscosity which ensures a smooth transition of viscosity at interface [30], which is described as

$$\frac{1}{\bar{\nu}} = \frac{\rho_r}{\rho_r + \rho_b} \frac{1}{\nu_r} + \frac{\rho_b}{\rho_r + \rho_b} \frac{1}{\nu_b}, \quad (6)$$

$\bar{\tau}$ is the relaxation time in standard BGK model and c_s is the lattice sound speed. Meanwhile, the relaxation parameter corresponds to the conserved moments, like density and momentum, and should ensure $S_\rho = S_j = 0$. Other parameters are adjusted to increase numerical stability [51,53]. Consequently in this paper, we select

$$\begin{aligned} S_\rho = S_j = 0, \quad S_\pi = S_\varepsilon = 1.0, \\ \frac{1}{S_e} = \frac{1}{S_v} = \tau = \frac{\nu_{\text{eff}}}{c_s^2 \delta t} + \frac{1}{2}, \quad (7) \\ S_m = 1.2, \quad S_q = 1.5. \end{aligned}$$

Here the ν_{eff} is the value of effective viscosity in the model. In normal models it can be the fluid viscosity value, but in the multiphase problem of this work, it should be calculated as the harmonic density weighted average viscosity $\bar{\nu}$. According to [30,33,46], the equilibrium distribution function \mathbf{f}^{eq} is the function of macroscopic variables given by

$$\begin{aligned} & f_i^{\text{eq}}(\rho, \mathbf{u}) \\ &= \rho \left[\phi_i + \varphi_i \bar{\alpha} + \omega_i \left(3\mathbf{e}_i \cdot \mathbf{u} + \frac{9}{2} (\mathbf{e}_i \cdot \mathbf{u})^2 - \frac{3}{2} \mathbf{u} \cdot \mathbf{u} \right) \right] + \Gamma_i, \end{aligned} \quad (8)$$

$$\Gamma_i = \bar{\nu} [\psi_i (\mathbf{u} \cdot \nabla \rho) + \xi_i (\mathbf{G} : \mathbf{e}_i \otimes \mathbf{e}_i)], \quad (9)$$

in which Γ_i is the correction term related to the density ratio; \otimes and $:$ denotes the tensor product and contraction, respectively. The tensor \mathbf{G} is defined by

$$\mathbf{G} = (\mathbf{u} \otimes \nabla \rho) + (\mathbf{u} \otimes \nabla \rho)^T. \quad (10)$$

The superscript T denotes the transpose operator. The ψ_i , ξ_i , ϕ_i , φ_i , and ω_i are lattice-dependent weights, and the specific

values of different lattices can be found in the Appendix of Ref. [30]. The parameter α is related to the density ratio between the two fluids [30,54],

$$\gamma_{rb} = \frac{\rho_r^0}{\rho_b^0} = \frac{1 - \alpha_b}{1 - \alpha_r}, \quad (11)$$

where the superscript represents the initial reference value. The parameter $\bar{\alpha}$ in the Eq. (8) denotes the arithmetic density weighted average [30],

$$\bar{\alpha} = \frac{\rho_b}{\rho_r + \rho_b} \alpha_b + \frac{\rho_r}{\rho_r + \rho_b} \alpha_r. \quad (12)$$

In the bulk region of fluid k , the pressure is $p_k = \rho_k (c_s^k)^2 = \rho_k \xi (1 - \alpha_k)$, where c_s^k is the isothermal sound speed of fluid k , and ξ is a lattice-dependent weight parameter related to the isothermal speed of sound; for D3Q19 it is $\xi = 0.5$. The ξ parameter is recommended to be consulted in the Appendix of Ref. [30]. In order to avoid unphysical negative pressure, we assume $\rho_b \leq \rho_r$ and let the free parameter α_k satisfies $0 < \omega_i = \alpha_b \leq \alpha_r < 1$.

To address interfacial tension, the perturbation operator is employed in the color-gradient model [30,54] as

$$\Omega_i^2 = A |\nabla C| \left[\frac{\omega_i (\nabla C \cdot e_i)^2}{|\nabla C|^2} - B_i \right], \quad (13)$$

where $C = (\rho_r - \rho_b)/(\rho_r + \rho_b)$ denotes the color function. B_i are lattice-dependent parameters, which should be well chosen to comply with the capillary stress tensor in the macroscopic equations [54]. Parameter A is related to the interfacial tension σ ,

$$A = \frac{9\sigma}{4\bar{\tau}}. \quad (14)$$

Although the perturbation operator successfully reproduces the macroscopic interfacial dynamics, fluid immiscibility cannot be guaranteed. Hence, the recoloring operator in Refs. [30,55] is applied to the postcollision distribution functions f_i^+ to prevent fluid mixing as

$$f_i^{++k}(\mathbf{x}, t) = \frac{\rho_k}{\rho} f_i^+ \pm \beta \frac{\rho_b \rho_r}{\rho^2} \cos(\psi_i) f_i^{\text{eq}}(\rho_k, 0), \quad (15)$$

where

$$\cos(\psi_i) = \frac{|\mathbf{e}_i \cdot \nabla C|}{|\mathbf{e}_i| |\nabla C|}. \quad (16)$$

To this point, we have established the LB framework for simulating immiscible multiphase flow with large density and viscosity ratio. However, the color-gradient model cannot capture liquid-vapor phase change spontaneously. For this reason, it is required to incorporate the pseudopotential model [18,41] to realize phase change, which will be introduced in the next section.

B. Pseudopotential model for phase change flow

As mentioned in the Introduction, we propose to incorporate the pseudopotential model [18,41] into the color-gradient model [17,30] to consider the phase-change phenomena of the immiscible multiphase flow. In the pseudopotential model, a nonlocal interaction force related to pseudopotential is employed to account for the nonideal gas effect which allows

the fluid phase change [18,41]. Without loss of generality, we assume that the fluid b (water, volatile hydrocarbons or carbon dioxide, hereinafter referred to as phase-change fluid) is more prone to phase change than fluid r (hereinafter referred to as non-phase-change fluid). Therefore, the interaction force in fluid b can be defined as [18,19]

$$\mathbf{F}_b^{\text{SC}}(x) = -\mathcal{G} \psi_b(x) \sum_i \omega(|e_i|^2) \psi_b(x + e_i) e_i, \quad (17)$$

where SC denotes pseudopotential model (proposed by Shan and Chen), Ψ denotes the pseudopotential, \mathcal{G} denotes the interaction strength, and $\omega(|e_i|^2)$ denotes the weight coefficient. For the D3Q19 lattice and the nearest-neighboring interaction scheme employed in this work, $\omega(1) = 1/6$ and $\omega(2) = 1/12$. Therefore, the equation of state for fluid b is [19,56]

$$p = \rho (c_s^b)^2 + \frac{c^2 \mathcal{G} \psi_b^2}{2}. \quad (18)$$

To achieve thermodynamic consistency, we employed Yuan and Schaefer [57] pseudopotential scheme along with the Li *et al.* [41,42] forcing scheme. The schemes are shown as follows:

$$\psi(\rho_b, T) = \sqrt{\frac{2(p_{\text{EOS}}(\rho_b, T) - \rho_b (c_s^b)^2)}{\mathcal{G} c^2}}, \quad (19)$$

$$\tilde{F}_i^{\text{SC}} = \omega_i \left(1 - \frac{\delta t}{2\tau} \right) \left[\frac{3(e_{i\alpha} - u'_\alpha)}{c^2} + \frac{9(e_{i\beta} u'_\beta)}{c^4} e_{i\alpha} \right] F_\alpha^{\text{SC}} \delta t, \quad (20)$$

where p_{EOS} is the pressure calculated via the equation of state, \tilde{F}_i^{SC} is the discrete Shan-Chen force term in the LB equation, $u' = \sum_i f_i e_i + F \delta t / 2\rho + \lambda F^{\text{SC}} / (v \psi^2)$ is the modified velocity, and λ is a constant adjustable parameter to achieve thermodynamic consistency [41,42] which is 0.11 in this study. It is worthwhile to note that the thermodynamic consistency is necessary to achieve the correction density relationship; otherwise, the density value especially the gas density value will be significantly overpredicted. Based on pseudopotential scheme defined by Eq. (19), the interaction strength \mathcal{G} does not affect the interaction force \mathbf{F}_b^{SC} provided that the term inside arithmetic square root is positive [41,42,57]. In this work, we employ $\mathcal{G} = -1$ for all cases.

For simplicity, we adopt the reduced form of the Peng-Robinson equation of state (PR EOS) which is widely applied in the literature [58–61],

$$p_{\text{EOS}}(\rho, T) = \frac{R_g T \rho}{1 - b\rho} - \frac{a\Phi(T)\rho^2}{1^2 + 2b\rho - b^2\rho^2}$$

$$\Phi(T) = \left[1 + (0.37464 + 1.54226\omega_a - 0.26992\omega_a^2) \right. \\ \left. \times (1 - \sqrt{T/T_c}) \right]^2, \quad (21)$$

where ω_a is the acentric factor, R_g is the gas constant, $a = 0.45724 R_g^2 T_c^2 / p_c$, $b = 0.07780 R_g T_c / p_c$, and T_c and p_c denote the critical temperature and pressure, respectively. In this work, a set of parameters commonly employed in the literature [41,62,63] is applied, $a = 2/49$, $b = 2/21$, $R_g = 1$, and $\omega_a = 0.344$ for water and $\omega_a = 0.225$ for carbon dioxide. According to theorem of corresponding states, simulation results

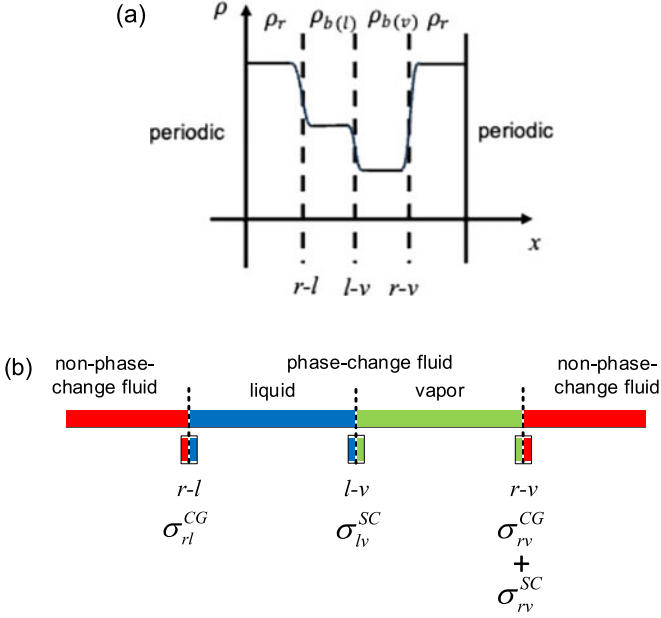


FIG. 1. Schematic diagrams of a three-phase flow system. (a) Density profile composed of fluid b undergoing liquid-vapor separation and fluid r . (b) Illustration at component and phases interfaces with different surface effect σ , the superscript represents effect from the model, the subscript represents the type of interfaces.

can be converted to the actual quantities (temperature, pressure, and density) via a trivial algebraic procedure [41,57].

C. Coupling method of color-gradient model and pseudopotential Model

The aforementioned procedure establishes the phase change model of fluid b . Nevertheless, the pseudopotential and the interaction force of the fluid r is undefined. Before we further provide the actual solution to this problem, a simple analysis is conducted to demonstrate the necessity of defining the pseudopotential and the interaction force for the fluid r .

Consider a three-phase system consisting of fluid r , liquid phase (denoted via l hereafter), and vapor phase (denoted via v hereafter) of fluid b . In this system, there are three interfaces: the l - v interface, the r - l interface, and the r - v interface displayed in Fig. 1. For a planar interface at steady state, the bulk pressure on both sides of the interface is identical. First, it supposes the pseudopotential and the interaction force is only defined for fluid b . Then the l - v interface and the r - l interface can be modeled by the pseudopotential model [18,19] and the color-gradient model [30,54], respectively. The interfaces are described as

$$\begin{aligned}
 l\text{-}v \text{ interface: } p_l^{\text{SC}} &= (c_s^b)^2 \rho_l + \frac{c^2 \mathcal{G}}{2} (\psi_l)^2 \\
 &= (c_s^b)^2 \rho_v + \frac{c^2 \mathcal{G}}{2} (\psi_v)^2 = p_v^{\text{SC}} \\
 r\text{-}l \text{ interface: } p_r^{\text{CG}} &= (c_s^r)^2 \rho_r = (c_s^b)^2 \rho_l = p_l^{\text{CG}}, \quad (22)
 \end{aligned}$$

where SC denotes Shan-Chen model and CG denotes the color-gradient model. Similarly, since there is no interaction force across the r - v interface, the pressure balance requires

$p_r^{\text{CG}} = p_v^{\text{CG}} = p_l^{\text{CG}}$, leading to $\rho_l = \rho_v$, which contradicts to the pseudopotential EOS. Most significantly, the system lacks a unified equation of state for the fluids, particularly for the liquid phase of fluid b .

Hence, in this paper, the pseudopotential is extended to the non-phase-change fluid as well. Meanwhile, the interaction force is introduced to the r - v interface and the r - l interface correspondingly. To avoid altering the original models of the l - v and r - l interfaces when introducing interaction forces at the r - v interface, we define $\Psi_r = \Psi_l$ at the bulk phase. Consequently, $F^{\text{SC}} = 0$ at the r - l interface, while F^{SC} is equal but in the opposite-direction l - v and r - v interfaces. Additionally, the equation of state of this system is defined as

$$p = \rho_k (c_s^k)^2 + \frac{c^2 \mathcal{G} \psi^2}{2}, \quad (23)$$

$$\psi = \psi(\rho_b, \rho_r, T). \quad (24)$$

It can be verified that this EOS consistent with the aforementioned three-phase system at the bulk region with $\psi_r = \psi_l$ and $(c_s^r)^2 \rho_r = (c_s^b)^2 \rho_l$. Moreover, $\Psi(\rho_b, \rho_r, T)$ should vary smoothly in the interface region due to the diffuse interface nature of the multiphase model. In this paper, we adopt the following scheme for the pseudopotential:

$$\psi(\rho_b, \rho_r, T) = \psi_k(\rho_b, T) + \psi_r(\rho_r, \text{eff}, T), \quad (25)$$

$$\psi_k(\rho_k, T) = \sqrt{\frac{2(p_{\text{EOS}}(\rho_k, T) - \rho_k (c_s^k)^2)}{\mathcal{G} c^2}}, \quad (26)$$

$$\rho_{r, \text{eff}} = \max\left(\frac{\rho_r}{\gamma_{rl}}, \rho_{l, \text{sat}} \left(\frac{\gamma_{rv}(C-1)+2}{2}\right)\right), \quad (27)$$

where $\rho_{r, \text{eff}}$ is the effective density of non-phase-change fluid r , $\gamma_{rm} = \rho_r / \rho_{m, \text{sat}}$ is the density ratio reference to saturated density of phase m of the phase change fluid b , and C is the color function in the color-gradient model. The derivation of this scheme and a discussion of other unsuccessful attempts are detailed in the Appendix.

Since both the color-gradient model and the pseudopotential model is applied at the r - v interface and contributes to the density ratio, the correction term Γ_i [30,46] is required to be modified into

$$\begin{aligned}
 \Gamma_i &= \bar{v} [\psi_i(\mathbf{u} \cdot \nabla \rho^{\text{CG}}) + \xi_i((\mathbf{u} \otimes \nabla \rho^{\text{CG}} \\
 &\quad + (\mathbf{u} \otimes \nabla \rho^{\text{CG}})^T) : \mathbf{e}_i \otimes \mathbf{e}_i)] \\
 \rho^{\text{CG}} &= \rho_r - \frac{\rho_r}{\gamma_{rl}}, \quad \rho^{\text{SC}} = \frac{\rho_r}{\gamma_{rl}} + \rho_b. \quad (28)
 \end{aligned}$$

Moreover, the interfacial tension $\sigma_{rv} = \sigma_{rv}^{\text{SC}} + \sigma_{rv}^{\text{CG}}$ according to $\Psi_r = \Psi_l$ and $\sigma_{rv}^{\text{SC}} = \sigma_{lv}$.

Finally, the r - l interface and the r - v interface have different interfacial tensions in order to incorporate different interfacial tension γ and recoloring parameter β for the r - v interface and the r - l interface separately (key parameters to in color gradient model phase separation), F^{SC} is adopted as the criterion to distinguish between the r - v interface and the r - l interface considering the $F^{\text{SC}} = 0$ at the r - l interface, the two

parameters in the model are selected as

$$\gamma = \begin{cases} \gamma^{rv} & |F^{\text{SC}}| \geq 10^{-2}, \\ \gamma^{rl} & |F^{\text{SC}}| < 10^{-2} \end{cases} \quad (29)$$

$$\beta = \begin{cases} \beta^{rv} & |F^{\text{SC}}| \geq 10^{-2} \\ \beta^{rl} & |F^{\text{SC}}| < 10^{-2}. \end{cases} \quad (30)$$

Since F^{SC} is generally on the order of 0.5, and the contribution to surface tension mainly comes from regions where ∇C and $\nabla \Psi$ are large, which coincide with areas where F^{SC} is also large, this paper sets $|F^{\text{SC}}| \geq 10^{-2}$ as the criterion. This does not introduce significant errors in the calculation of surface tension.

The coupling method proposed above is based on a single-component equation of state which means it assumes the liquid and vapor phases of the phase change component follows the same equation of state. For some real cases that needs multicomponent, a similar coupling method can be introduced by considering more interface interactions between the different phases and components and they can follow different equations of state. However, it also means a complex interface treatment and larger computation costs.

The temperature field that used to support the phase change is described as Ref. [64]. The corresponding thermal LB equation was given by

$$g_\alpha(x + e_\alpha \delta_t, t + \delta_t) - g_\alpha(x, t) = -\frac{1}{\tau_g} (g_\alpha - g_\alpha^{\text{eq}}) + \delta_t G_\alpha, \quad (31)$$

where g_α is the temperature distribution function, τ_g is nondimensional relaxation time for the temperature field, and the source term $G_\alpha = \omega_\alpha \phi$, in which ϕ is described as

$$\phi = T \left[1 - \frac{1}{\rho c_v} \left(\frac{\partial p_{\text{EOS}}}{\partial T} \right)_\rho \right] \nabla \cdot \mathbf{v}. \quad (32)$$

The equilibrium temperature distribution function g_α^{eq} was given by

$$g_\alpha^{\text{eq}} = \omega_\alpha T \left[1 + \frac{\mathbf{e}_\alpha \cdot \mathbf{v}}{c_s^2} + \frac{\mathbf{v} \mathbf{v} : (\mathbf{e}_\alpha \mathbf{e}_\alpha - c_s^2 \mathbf{I})}{2c_s^4} \right], \quad (33)$$

where \mathbf{I} is the unit tensor and c_v is the specific heat at constant volume and the thermal diffusivity $\chi = \lambda / \rho c_v$, with thermal conductivity λ at the local node.

III. VERIFICATIONS

In this section, a series of benchmarks are conducted to verify the proposed method by comparisons with theoretical models.

A. Liquid-vapor coexistence

For a phase-change model, the most fundamental validation lies in verifying its thermodynamic consistency [35,41,57]. In other words, it is necessary to verify the accuracy of the simulated densities of the saturated liquid and vapor phases against those predicted by the equation of state during liquid-vapor coexistence. The stationary droplet test is adopted to verify the liquid-vapor coexistence. Initially a

liquid droplet with a radius of $R_0 = 25$ surrounded by vapor phase is placed at the center of a computational domain of sized 100^3 . In the non-phase-change fluid, fluid r is not involved in this benchmark. Periodic boundary condition is applied at all domain boundaries. The initial density distribution is [41]

$$\rho(\mathbf{x}) = \frac{\rho_l + \rho_v}{2} - \frac{\rho_l - \rho_v}{2} \tanh\left(\frac{2(R - R_0)}{w}\right), \quad (34)$$

where $w = 5$ denotes the initial interface width, $R = \sqrt{(x - x_0)^2 + (y - y_0)^2 + (z - z_0)^2}$, and (x_0, y_0, z_0) is the center of the computational domain. The coexistence curve of the cases $\tau = 0.6$ and $\tau = 0.8$ is presented in Fig. 2. The error is analyzed with MRT results. The average relative density error at the same reduced temperature of case $\tau = 0.6$ and $\tau = 0.8$ at the gas phase are 5.53×10^{-2} and 5.89×10^{-2} . The average relative density error at the liquid phase for the two τ cases are 7.87×10^{-3} and 1.55×10^{-2} . The relative error of gas phase is significantly higher than the liquid phase. The parameter $\lambda = 0.12$ for Li *et al.* forcing scheme [41] is employed for all cases. Our simulated results agree well with those predicted via the Maxwell construction with the lowest reduced temperature about $T/T_c = 0.7$, indicating our model is capable of accurately simulating single-component phase equilibrium. Figure 2(c) shows the pressure difference between the inside and outside of droplets with different radius at various reduced temperatures, further validating the Young-Laplace law.

B. Droplet evaporation

To further validate the accuracy of the phase-change algorithm, we also simulate the evaporation process of a single droplet [64]. As shown in Fig. 3(a), an initial droplet with a diameter of 80 is placed at the center of a computational domain of size 200^3 . The liquid phase inside the droplet has a density of $\rho_l = 6.50$, while the surrounding vapor phase has a density of $\rho_v = 0.38$, both at saturated state with $T_{\text{sat}} = 0.86T_c$. Similarly to the first benchmark, the boundaries of the flow field are all periodic. The temperature field is solved using the LBM scheme from Ref. [64], and the physical properties, initial conditions and boundary conditions are identical to those in Ref. [64]. Initially, the liquid phase is at the saturation temperature $T_l = T_{\text{sat}}$, while the vapor phase is at a temperature higher than that of the liquid phase. Two cases are simulated with superheat of $\Delta T = 0.14T_c$ and $\Delta T = 0.10T_c$. The boundary conditions of the temperature field are isothermal, with the temperature matching that of the vapor phase. Constant properties are adopted with the specific heat capacity $c_v = 5.0$, thermal conductivity is $k = 2/3$, and the kinematic viscosity is $\nu = 0.1$.

Simulation results are displayed in Fig. 3(b), which demonstrates good agreement with the D^2 law of the evaporation process, indicating that the current phase-change model can accurately simulates the phase-change process between liquid and vapor.

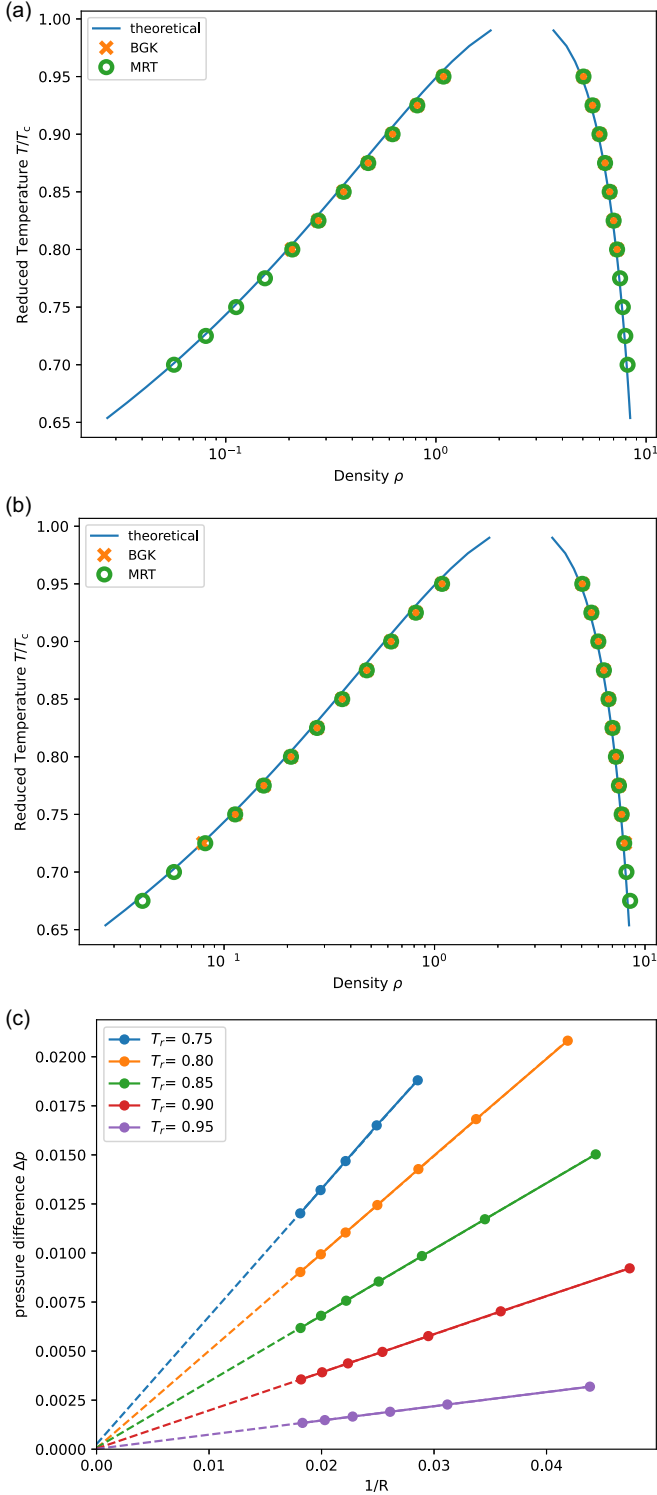


FIG. 2. Validation of single-component phase equilibrium. Comparison of the saturated density obtained from the Peng-Robinson equation with theoretical values: (a) $\tau = 0.6$ and (b) $\tau = 0.8$. (c) Benchmark on Young-Laplace law at different temperatures. $\tau = 0.8$.

C. Three-phase interfacial tension

Since the color gradient model for immiscible two-phase flows has been validated and applied in numerous studies [30,33,46], standard benchmarks including Young-Laplace

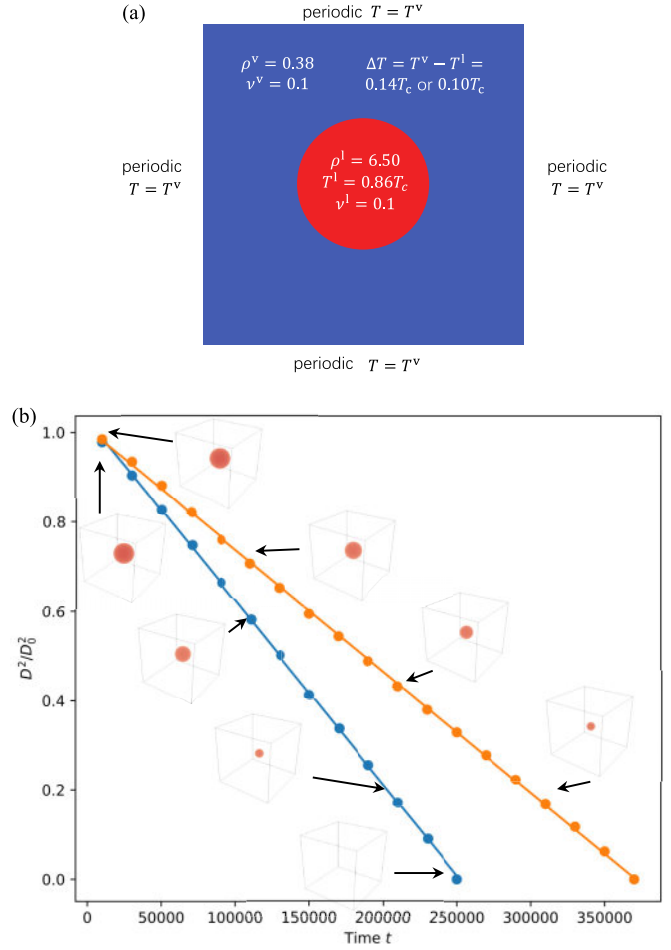


FIG. 3. Simulation of droplet evaporation process. (a) Schematic diagram of the simulation setup; (b) variation of the droplet diameter over the simulation time (sphere in cube). Blue dots are simulation results of $\Delta T = 0.14T_c$ and the blue line represents their linear fitting results. Orange dots are simulation results of $\Delta T = 0.10T_c$ and the orange line represents their linear fitting result.

benchmark and single channel displacement can be found in our pervious papers [29]. In this paper, we primarily focus on validating the accuracy of three-phase system formed by the coupled multiphase model.

For that purpose, we first present the benchmark on Neumann triangle which verifies the three-phase interfacial tension [46,65]. As Fig. 4 displays, the interfacial tensions at equilibrium satisfy the Neumann triangle if the three-phase junction point exists for a three-phase system. The equilibrium contact angle is related to the interfacial tension via [46,65]

$$\cos(\theta_{mn}) = \frac{\sigma_{mk}^2 + \sigma_{nk}^2 - \sigma_{mn}^2}{2\sigma_{mk}\sigma_{nk}}.$$

Here m , n , and k represent different fluid phases; θ_{mn} denotes the contact angle between phase m and phase n ; and σ_{mn} represents the interfacial tension between phase m and phase n .

Our simulation system is shown in Fig. 5. In order to measure the contact angle accurately, this benchmark is conducted in two-dimensional (2D) with a computational domain size of 400^2 . As is shown in Fig. 5(a), a droplet of non-phase-change

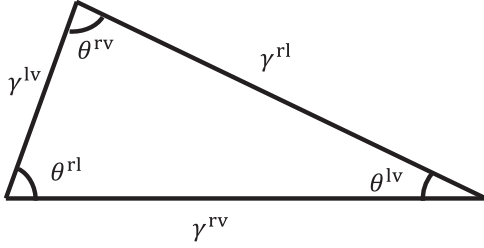


FIG. 4. Schematic diagram of the Neumann triangle. It is important to note that for the liquid (l)-liquid (l)-gas (g) three-phase system considered in this paper, the magnitudes of the interfacial tensions are not arbitrary. For example, in a water (w)-oil (o)-gas (g) system, the typical relationships are $\sigma_{gw} \geq \sigma_{wo} \geq \sigma_{go}$ and $\sigma_{gw} \approx \sigma_{wo} + \sigma_{go}$ [66].

fluid (red) with a diameter of 60 is placed at the center of the computational domain, surrounded by liquid (blue) and vapor (green) phases, each occupying half of the surrounding space. The phase-change fluid is at saturated state. The top and bottom boundaries are solid walls, while the remaining boundaries are periodic. Due to the interfacial tension, the central droplet of non-phase-change fluid will move to its equilibrium position. In this benchmark, we set $\rho_r = 10.0$, $\rho_l = 5.9$, and $\rho_v = 0.58$. The kinematic viscosity of the three fluids is identical, with $\nu = 0.4$. Since the interfacial tension and the density ratio is related to the temperature in the pseudopotential model, we set to $T = 0.9T_c$, with interfacial tensions $\sigma_{lv} = \sigma^{SC} = 0.099$, $\sigma_{rl} = 0.215$, and $\sigma_{rv} = 295$. The current interfacial tension setup has the same contact angles as the *n*-decane/*n*-decane vapor/water three-phase system commonly used in experiments [66,67].

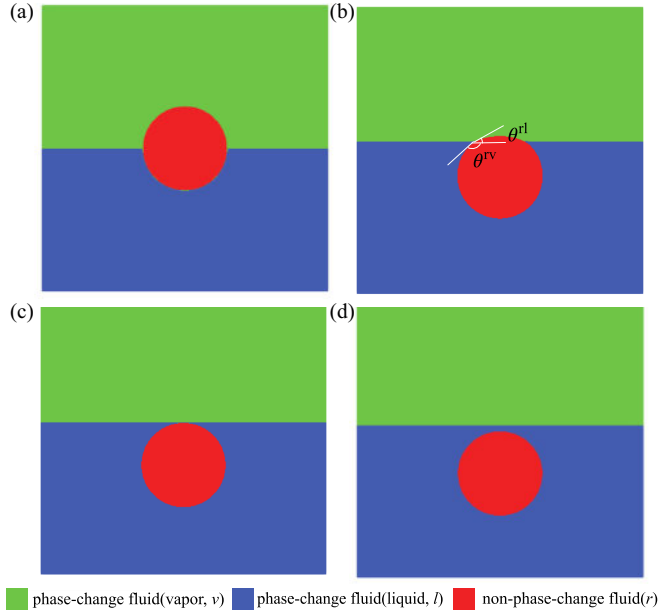


FIG. 5. Validation of the three-phase Young-Laplace law. (a) Initial state; (b) partial spreading ($\sigma_{lv} + \sigma_{rl} > \sigma_{rv}$), with $\sigma_{lv} = 0.099$, $\sigma_{rl} = 0.215$, $\sigma_{rv} = 0.295$; (c) exactly full spreading ($\sigma_{lv} + \sigma_{rl} = \sigma_{rv}$), with $\sigma_{lv} = 0.099$, $\sigma_{rl} = 0.15$, $\sigma_{rv} = 0.245$; (d) complete spreading ($\sigma_{lv} + \sigma_{rl} < \sigma_{rv}$), with $\sigma_{lv} = 0.099$, $\sigma_{rl} = 0.15$, $\sigma_{rv} = 0.299$.

Simulation result is displayed in Fig. 5(b), with the simulated angles $\theta_{rv} = 139.7^\circ$, $\theta_{rl} = 28.7^\circ$, and a maximum error of less than 5% compared to the theoretical solution. Figures 5(c) and 5(d) also displays simulation results of the complete spreading states (i.e., where the interfacial tensions cannot form a triangle) [65], specifically simulating the cases where the red fluid droplet is either tangent to or completely detached from the *l*-*v* interface, both in good agreement with the theory. These results indicate that the current model can accurately simulate the three-phase Young-Laplace law.

D. Multilayer Couette flow

To further validate the accuracy of multiphase momentum transport, we conduct the two-dimensional multilayer Couette flow benchmark [32,46]. As shown in Fig. 6, the computational domain size is 30×100 , with the top boundary set as the velocity boundary at $u_w = 0.01$, implemented via the nonequilibrium bounce-back (Zou-He) scheme [68], while the bottom boundary is a no-slip solid wall via the standard bounce-back collision, and the remaining boundaries are periodic. In this benchmark, we set $\rho_r = 10$ and $\nu_r = 0.1$ while the phase-change fluid is at $T = 0.86T_c$, with $\rho_l = 6.5$ and $\rho_v = 0.38$, and $\nu_l = \nu_v = 0.5$. Two types of fluid distribution is simulated, i.e., red-blue-green-red and red-green-blue-red, from top to bottom. At steady state, the momentum distribution across the cross-section is shown in Fig. 6. The proposed modified correction term [i.e., Eq. (28)] matches the analytical solution well [46], demonstrating that the current model can accurately simulate three-phase layered Couette flow while the original correction term [33] cannot be directly applied to the immiscible multiphase phase-change systems.

IV. RESULTS AND DISCUSSION

In this section, we apply the proposed model to investigate the phase change effect on immiscible multiphase displacements in porous media. As mentioned in the Introduction, such a process could happen extensively in numerous industrial applications [1–5]. Based on the extensive review of existing literature, our study marks the pioneering effort in conducting pore-scale direct numerical simulations specifically targeting immiscible multiphase displacements that encompass phase change. Furthermore, we delve into the impact of liquid-vapor phase change, a phenomenon that has received limited attention in the previous works, thereby contributing insights into this complex fluid dynamics process.

A. Numerical setup

In this work, two types of displacements are considered: (1) phase-change fluid being displaced by a non-phase-change fluid and (2) vice versa. There is a similar scenarios such as volatile oil being displaced by water in oil recovery [1] and liquid carbon dioxide displacing underground water in carbon geological sequestration [3,4], respectively. In order to provide a simple and common case verification for the experiments in the future, the phase change material is set as water. The numerical setup is illustrated in Fig. 7.

For the phase-change fluid displaced by the non-phase-change fluid case, the computational domain size is $1600 \times$

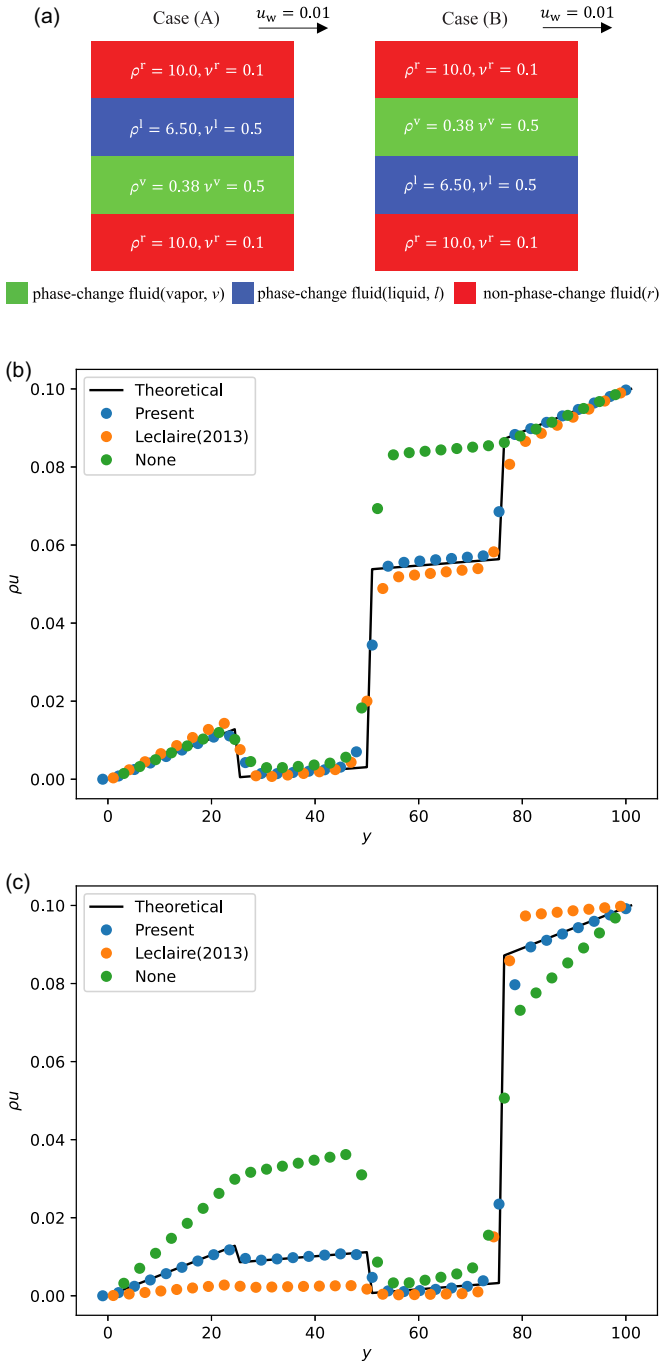


FIG. 6. Three-phase layered Couette flow validation. (a) Schematic diagram of the simulation setup; (b) cross-sectional momentum distribution at steady state for Case 1; (c) cross-sectional momentum distribution at steady state for Case 2. Leclaire (2013) is from Ref. [33].

800. To ensure computational stability, buffer zones of 100 and 1800 are added at the inlet and outlet, respectively. Initially, the porous medium is at a high temperature of $T = 0.98T_c$, and the phase-change fluid inside is in a saturated liquid state. Due to temperature and pressure changes in the reservoir, the system temperature decreases to $T = 0.90T_c$, causing the phase-change fluid to transition from a saturated state to a superheated state, resulting in phase change. The

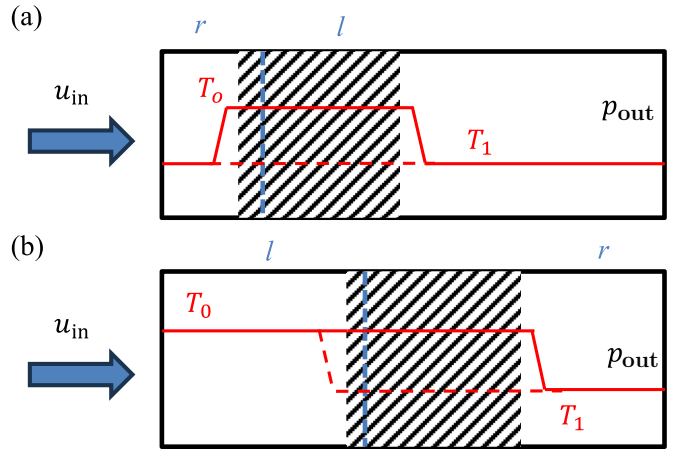


FIG. 7. Schematic diagram of the simulation setup for non-phase-change fluid displacing phase-change fluid in (a) and vice versa in (b).

inlet boundary is the velocity boundary, while the outlet boundary is the pressure boundary with an outlet pressure of $p_{out} = 0.44p_c$, slightly lower than the saturation pressure at $T = 0.90T_c$. At $T = 0.90T_c$, $\rho_r = 10.0$, $\nu_r = 0.1$ while $\rho_l = 5.90$, $\rho_v = 5.90$, and $\nu_l = \nu_v = 0.4$. The interfacial tension $\sigma_{lv} = \sigma^{SC} = 0.099$, $\sigma_{rl} = 0.215$, and $\sigma_{rv} = 295$. The contact angles to the solid wall are all 90° .

Similarly, the computational domain size of the non-phase-change fluid displaced by the phase-change fluid case is 1600×800 , while the buffer size of the inlet and outlet is 300 and 1800, respectively. Initially the temperature of the porous medium region is at $T = 0.98T_c$ and decreases to $T = 0.90T_c$ when the saturation of the displacing fluid is $S_{in} = 45\%$. The inlet boundary is a velocity boundary where the liquid phase of the phase-change fluid flows in, while the outlet boundary is a pressure boundary with an outlet pressure of $p_{out} = 0.44p_c$. Here the non-phase-change fluid is assumed to have a higher kinematic viscosity, we set $\nu_r = 0.4$ while $\nu_l = \nu_v = 0.1$. Other properties are identical to those of the former case.

Since this work primarily focuses on the impact of phase change induced by temperature and pressure variations in the reservoir environment, it is assumed that during the displacement process, the system temperature equals the environmental temperature, and the effect of flow on the temperature field is not considered.

B. Phase-change fluid displaced by non-phase-change fluid

The phase distribution results of the phase-change fluid displaced by the non-phase-change fluid are presented in Fig. 8. with an inlet velocity of $u_{in} = 1 \times 10^{-5}$. For comparison, the results without the phase-change process are obtained via the color-gradient model with the same parameters. It can be observed that, during the early stage of the simulation, due to the temperature decrease in the system, the fluid in the porous medium region becomes superheated, forming a large number of bubbles inside the porous medium. Additionally, since the outlet pressure is lower than the saturation pressure at that temperature, a gas layer forms at the end of the porous medium. In comparison, such phase change

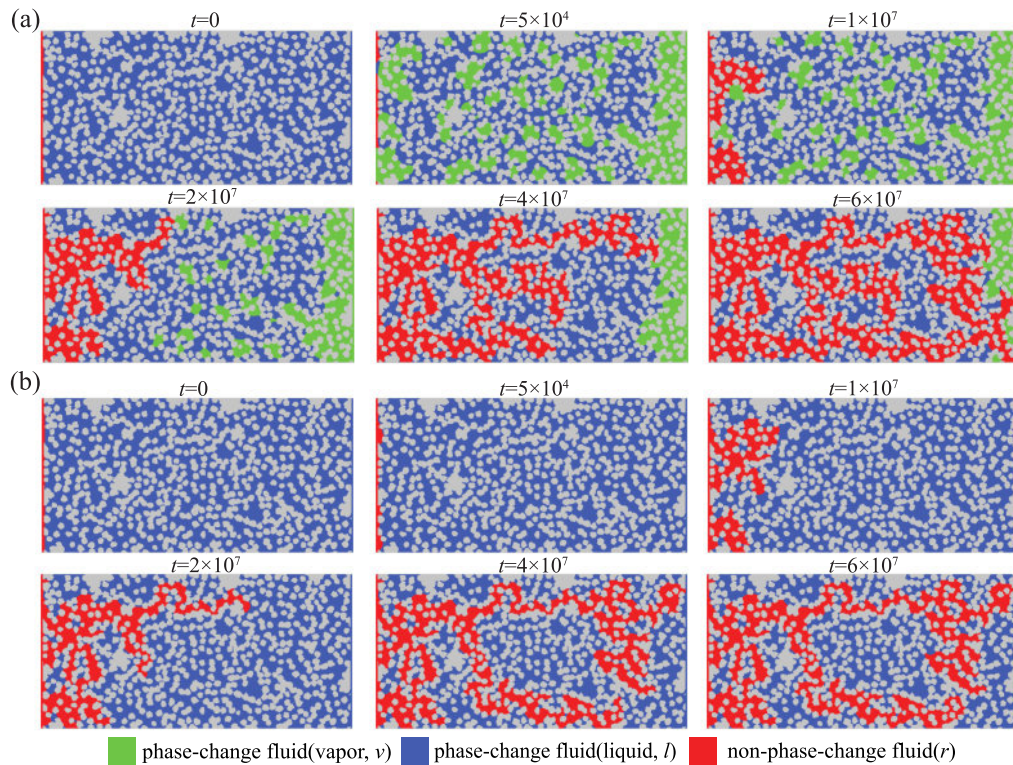


FIG. 8. Simulation of phase distribution over time during the displacement of phase-change fluid by non-phase-change fluid. (a) With the phase-change process considered; (b) without the phase-change process considered. The inlet velocity is $u_{in} = 1 \times 10^{-5}$, and the capillary number is $Ca = 5 \times 10^{-5}$.

phenomenon cannot be captured by the former color-gradient model.

As the displacement time increases, the number of interfaces within the porous medium increases, leading to an increase in capillary pressure and fluid pressure, resulting in a decrease in both the number and volume of bubbles within the porous medium. After breakthrough, gas remains only at the end of the porous medium.

Moreover, due to the presence of gas, the displacement path with phase change differs significantly from that without phase change. Noted that $\sigma_{rv} > \sigma_{rl} > \sigma_{lv}$, the local capillary

force is greater when the non-phase-change fluid (red) contacts the vapor phase (green) than when it contacts the liquid phase (blue). This blocks the displacement front, causing the variation in the displacement path. This phenomenon cannot be captured by simulations without phase change model. Figure 9 demonstrates the change in displacement path caused by bubble blockage during the displacement process. As illustrated, due to the heterogeneity of the microscopic pore structure, preferential flow is formed in the result without considering phase change. However, in the simulation with phase change, the presence of bubbles blocks the preferential

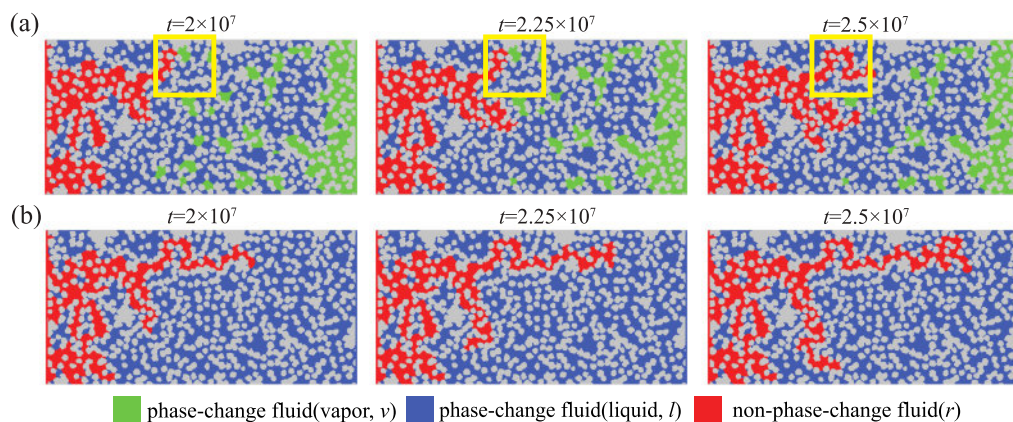


FIG. 9. Simulation of the internal bubble blockage during the displacement of phase-change fluid by non-phase-change fluid. (a) With the phase-change process considered; (b) without the phase-change process considered. The inlet velocity is $u_{in} = 1 \times 10^{-5}$, and the capillary number is $Ca = 5 \times 10^{-5}$. The yellow-framed areas indicate the bubble blockage regions.

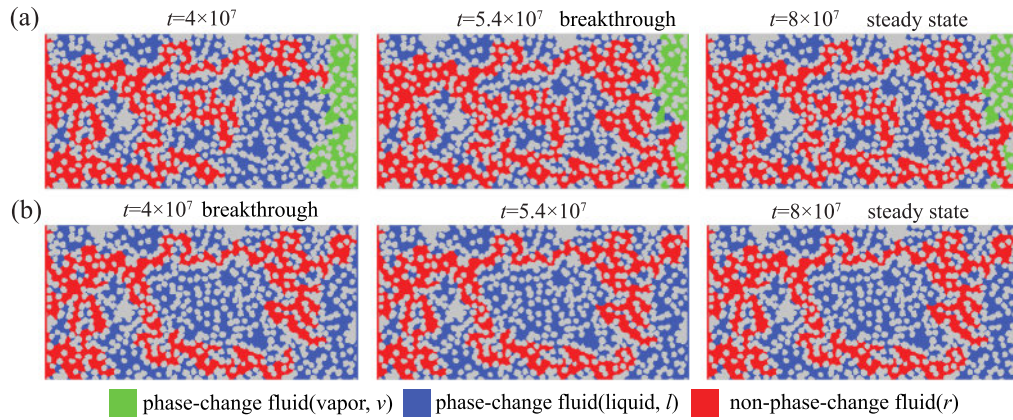


FIG. 10. Simulation of the breakthrough process during the displacement of phase-change fluid by non-phase-change fluid. (a) With the phase-change process considered; (b) without the phase-change process considered. The inlet velocity is $u_{in} = 1 \times 10^{-5}$ and the capillary number is $Ca = 5 \times 10^{-5}$.

flow, resulting in different displacement path. However, such blockage is not permanent. As the pressure increases, the bubbles phase-change back into the liquid phase and the blockage effect disappears. Then the non-phase-change fluid continues to displace along the original preferential flow path. Therefore, this gas blockage effect depends on the local pressure within the pore and relates to the actual pore structure, fluid properties, and flow conditions.

Additionally, the gas layer at the end of the porous medium can also have a similar blockage effect, as shown in Fig. 10. Due to the presence of the gas layer, the displacement paths with phase change are different from those without phase

change. However, it is important to note that since the outlet boundary pressure is constant, the gas layer remains stable at low Ca and does not disappear over time. Consequently, different breakthrough positions are formed.

As the flow rate increases, the viscous force grows, raising the pressure within the porous medium, making it difficult for the gas to remain stable during displacement. Therefore, at higher flow rates, gas-blockage effect may become insignificant. The simulation results of non-phase-change fluid displacing phase-change fluid under different inlet flow rates (capillary numbers) is presented in Fig. 11. It can be observed that in cases with higher capillary numbers ($Ca = 5 \times 10^{-4}$),

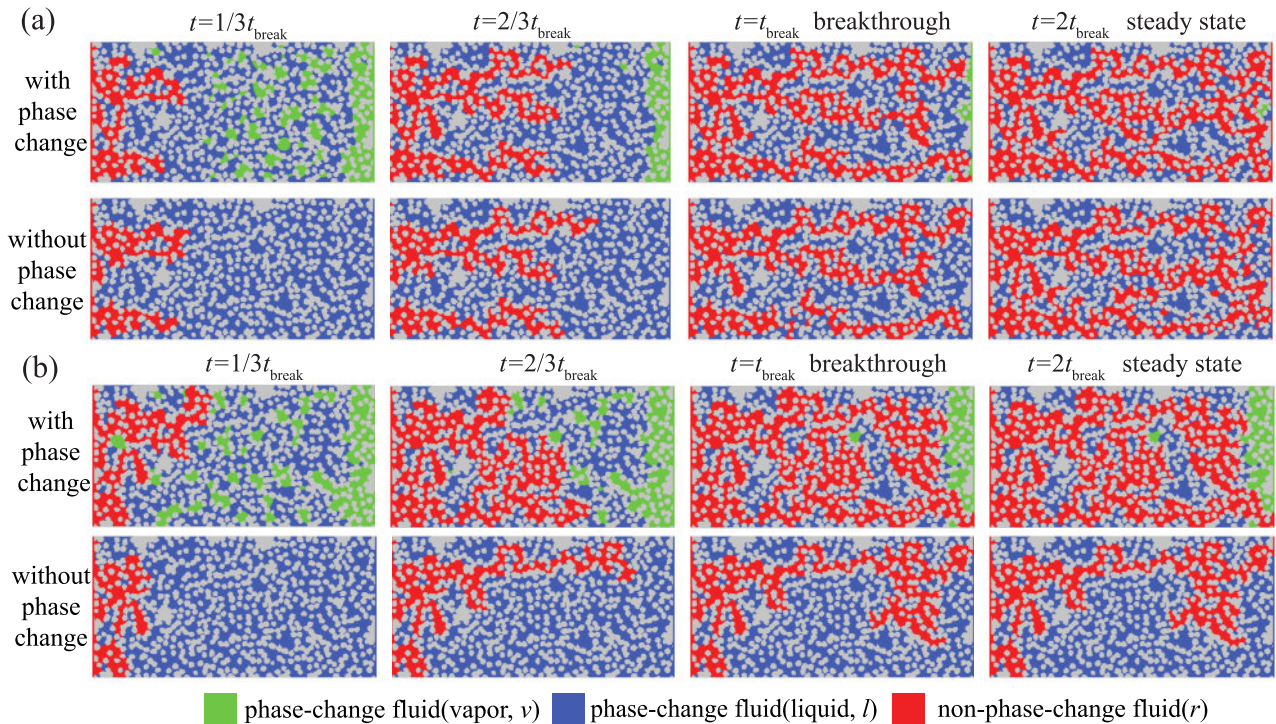


FIG. 11. Simulation results of non-phase-change fluid displacing phase-change fluid at different flow rates. (a) Inlet velocity $u_{in} = 1 \times 10^{-4}$, capillary number $Ca = 5 \times 10^{-4}$; (b) inlet velocity $u_{in} = 2 \times 10^{-6}$, capillary number $Ca = 1 \times 10^{-5}$. The results for inlet velocity $u_{in} = 1 \times 10^{-5}$ and capillary number $Ca = 5 \times 10^{-5}$ can be found in Fig. 8.

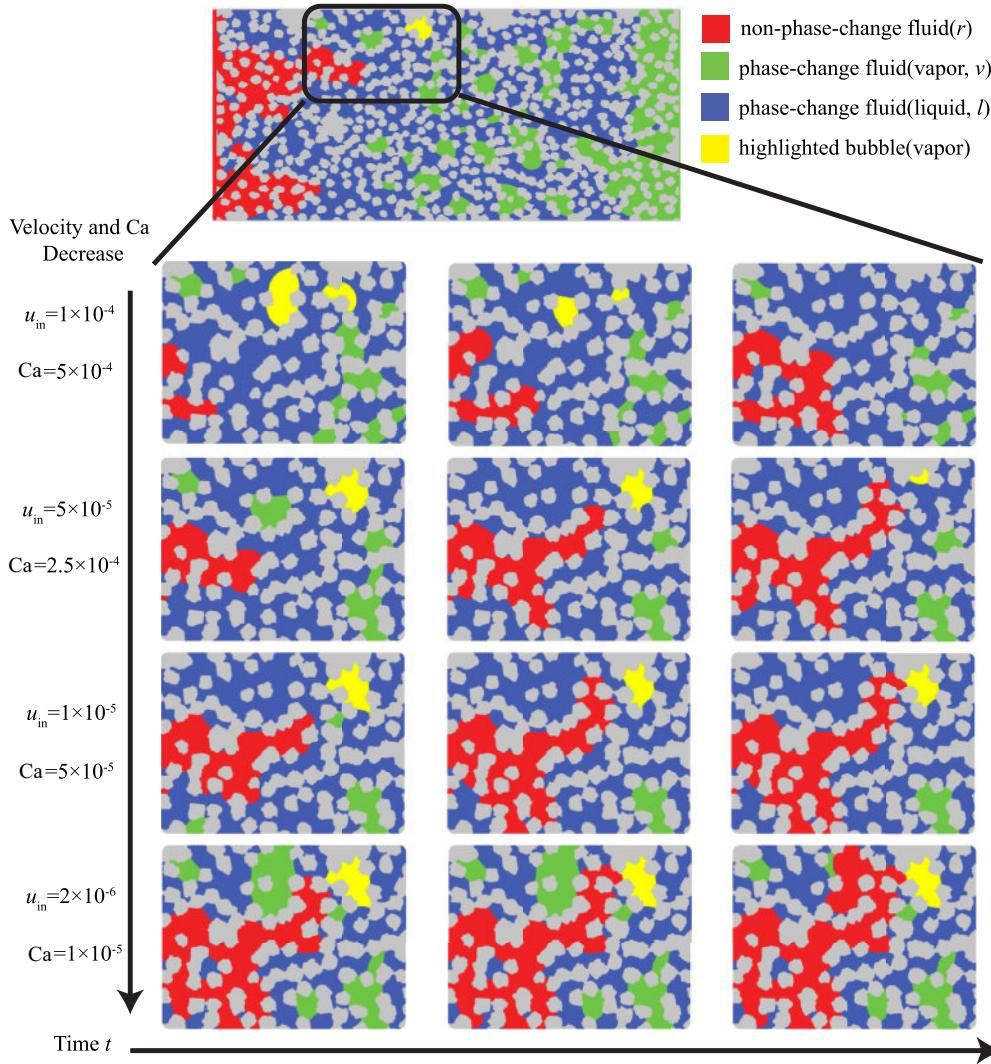


FIG. 12. Local gas blockage/phase-change processes during the displacement of phase-change fluid by non-phase-change fluid at different flow rates.

the displacement path is similar to the simulation results without considering the phase-change process, and the gas-blockage effect is not evident. However, at lower capillary numbers ($Ca = 1 \times 10^{-5}$), the gas-blockage effect is significant, effectively suppressing the preferential flow at low Ca , leading to a noticeable change in the displacement path.

We also present a local view of the gas-blockage under different velocity conditions in Fig. 12 to further demonstrate the velocity effect. In the cases with low capillary numbers ($Ca = 1 \times 10^{-5}$ and $Ca = 5 \times 10^{-5}$), the bubbles did not undergo phase change, thereby inhibiting the preferential flow; whereas at higher capillary numbers, the bubbles undergo phase change before the displacement front reaches, resulting in the two-phase flow. Thus, the bubbles did not affect the flow path, i.e., the phase distribution at the breakthrough state and the steady state is similar to the simulation results without considering the phase-change process as Fig. 12 displays.

Thereafter, in order to provide more quantitative results, the displacement front position and the vapor saturation of

the displaced phase under different Ca is displaced in Fig. 13. In contrast, simulation results without considering the phase-change process are also provided in Fig. 13 as well. As shown in Fig. 13(a), the displacement front in the phase-change simulation lags significantly behind that in the simulation without phase change at low Ca , while at high Ca , the results of both simulations are closer. Moreover, due to the gas blockage effect on the preferential flow, there are more plateau regions in the phase-change simulation results, where the displacement front does not advance with the injection of the displacing fluid. This occurs because the gas blockage effect causes the displacement front to become stationary, forcing the fluid to displace along alternative paths. Figure 13(b) further demonstrates the variation of the vapor saturation, where a lower Ca results in a slower decrease in vapor saturation, indicating that the gas remains in the porous medium for a longer time, resulting large possibility of gas blockage. We also present the fluid saturation and the volume of the largest cluster of the displaced fluid at the steady state in Fig. 14. At low Ca , the saturation of the displaced fluid is lower, and the maximum

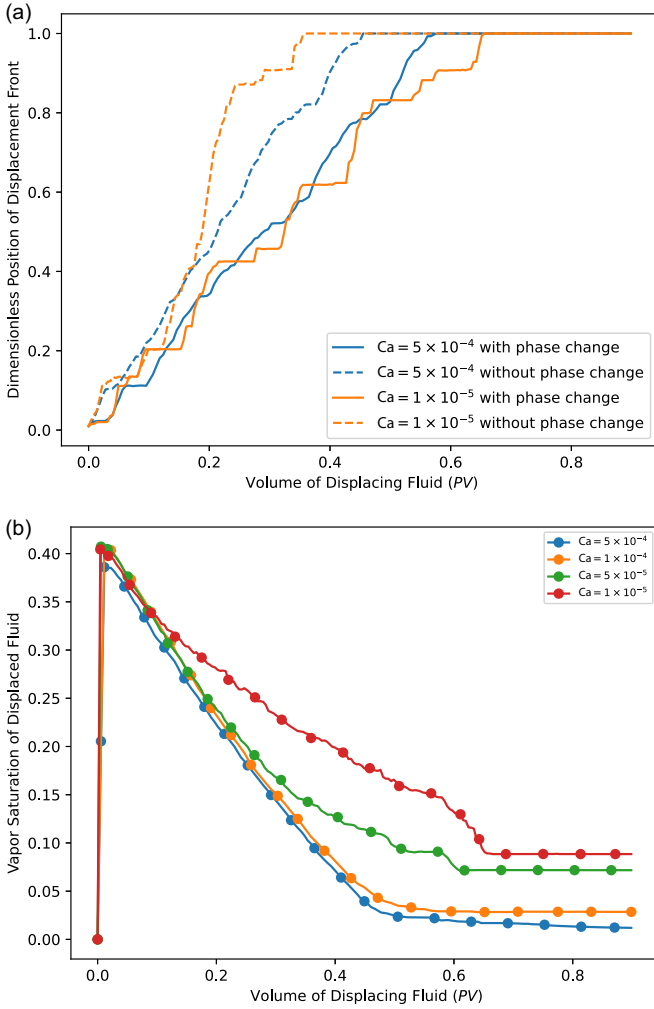


FIG. 13. The displacement front and the vapor saturation of the displaced fluid (phase-change fluid) with varying injected volumes of the displacing fluid at different capillary numbers. (a) The displacement front as the injected volume increases; (b) vapor saturation of the displaced fluid (phase-change fluid) as the injected volume of the displacing fluid increases.

microcluster volume is smaller in the phase-change simulation, indicating that the phase-change process effectively suppresses the preferential flow, resulting in a more thorough displacement. However, at high Ca , both the displaced fluid saturation and the maximum fluid microcluster volume in the phase-change simulation are similar to the results without considering the phase-change process.

C. Non-phase-change fluid displaced by phase-change fluid

Simulation results of the non-phase-change fluid and phase-change fluid is displaced in Fig. 15 with an inlet velocity of $u_{in} = 1 \times 10^{-4}$. For comparison, two cases without considering the phase-change process are set as control groups. In the first group, the fluid densities correspond to the case where $T = 0.98T_c$, with $\rho_b = 4.0$ and $\rho_r = 6.78$. In the second group, the fluid densities correspond to the case where $T = 0.90T_c$, with $\rho_b = 5.9$ and $\rho_r = 10.0$. To maintain

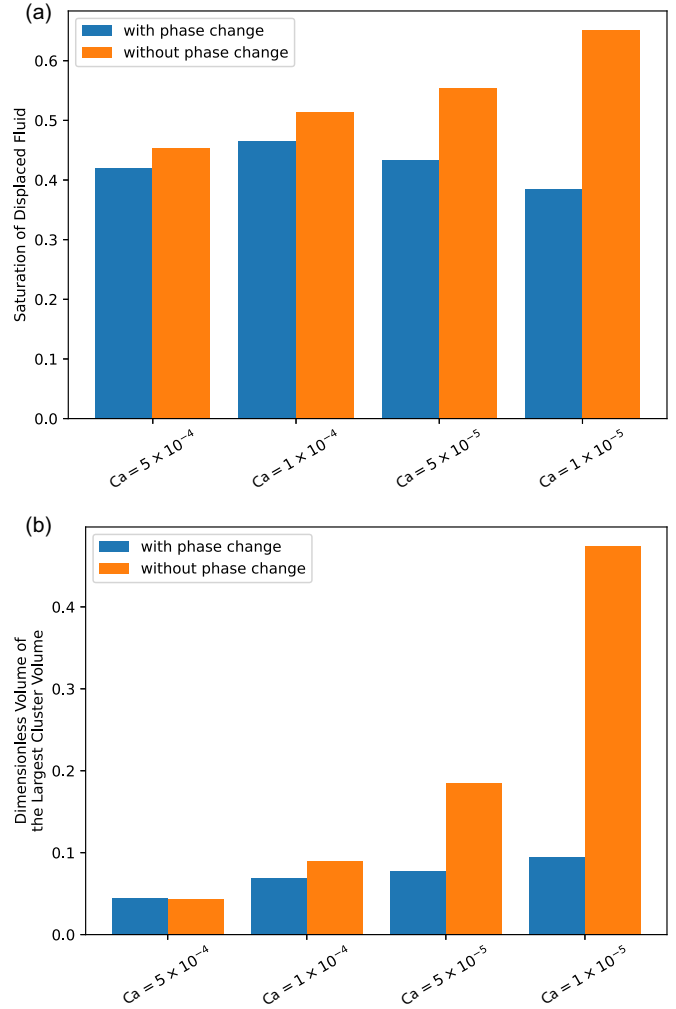


FIG. 14. Saturation of the displaced phase fluid after reaching steady state in (a) and the maximum dimensionless volume of the microdroplets in (b).

a constant inlet mass flow rate, the inlet velocity is adjusted to $u'_{in} = 0.678u_{in}$. These two control groups respectively represent the scenarios where the phase-change fluid displaces the non-phase-change fluid at different temperatures, but without considering the phase-change process. For simplicity, these will be referred to as group 1 and group 2 in the following discussion.

Since the flow rates in the control group differ in the simulation, results are presented in dimensionless displacing time, i.e., pore volume (PV). As the displacement progresses to a certain saturation level, the temperature drop leads to the phase change in the displacing fluid. The closer to the outlet, the lower the pressure and the greater the vapor saturation. Similarly, due to $\sigma_{rv} > \sigma_{rl} > \sigma_{lv}$, the displacement is temporarily blocked in the phase change case. As the displacement continues, the vapor undergoes phase change back to liquid, and the displacement proceeds in the form of two-phase flow. This phase-change process cannot be simulated by the former color gradient model. Additionally, at the same PV , the displacement front in the simulation with-

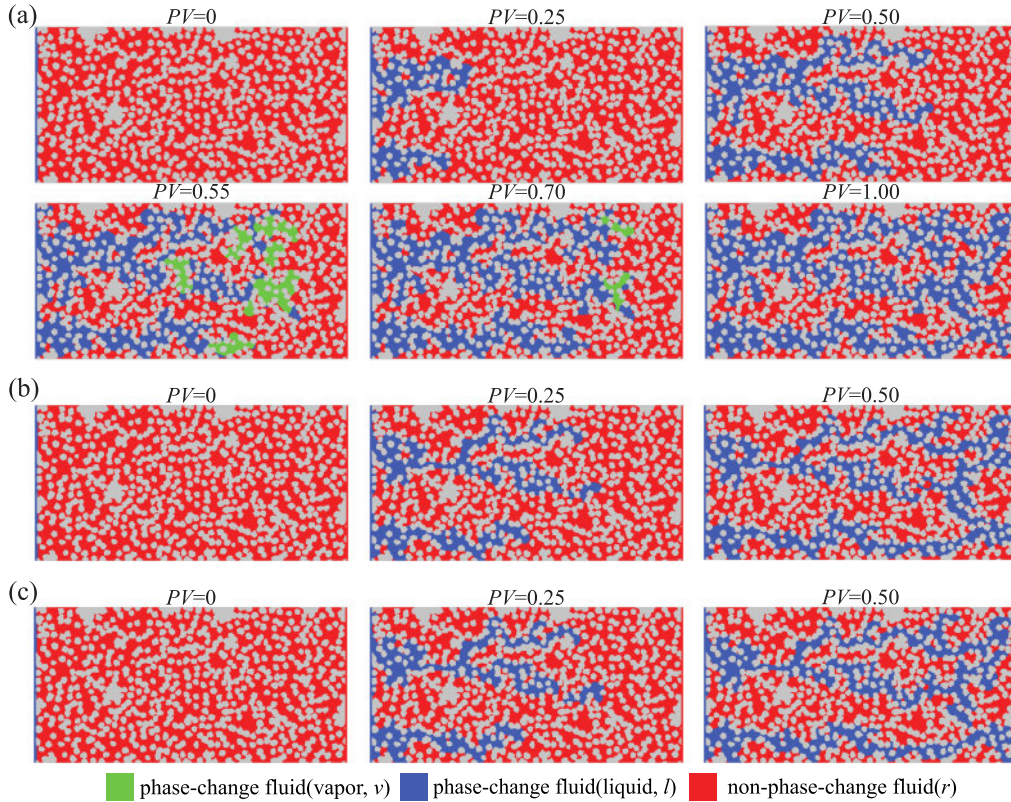


FIG. 15. The phase distribution in the simulation of phase-change fluid displacing non-phase-change fluid over time. (a) With phase-change process considered; (b) without phase-change (Group 1) at fluid density corresponding to saturation density at $T = 0.98T_s$; (c) without phase-change (Group 2) at fluid density corresponding to saturation density at $T = 0.90T_s$. The inlet velocity is $u_{in} = 1 \times 10^{-4}$, and the capillary number is $Ca = 2 \times 10^{-4}$.

out phase change is closer to the outlet and advances more quickly.

Figure 16 demonstrates the saturation variation of the displacing and displaced phases with dimensionless time PV . It can be observed that the saturation changes in the phase change case lag behind the results from the simulation without considering phase change, due to different gas compressibility between the two multiphase models. Additionally, because of the temperature variation, both the displacing fluid's liquid phase and the displaced fluid experience an increase in density, i.e., a decrease in saturation, which is reflected in the saturation jump shown in the figure. This saturation transition cannot be captured in the simulation without considering the phase-change process. After prolonged displacement, the saturation of the displaced fluid is lower in the phase-change simulation compared to the control groups, indicating higher displacement efficiency. This demonstrates the importance of considering phase change in simulating the displacement of non-phase-change fluid by phase-change fluid. Moreover, the results from the two control groups are similar due to the identical Ca , even though the inlet velocities are different.

To further explain the differences in gas compressibility between the presented model and the traditional color-gradient model, Fig. 17 illustrates the EOS at different temperatures

of the displacing fluid via the proposed model in this study, compared with the traditional color-gradient model. The multiphase-phase change model adopts the Peng-Robinson EOS for real fluids, whereas the color gradient model, consistent with other isothermal LBM models, uses the ideal gas EOS where temperature remains constant [30]. As displayed in Fig. 17, it is important to mention that the liquid phase of a real fluid also exhibits significant compressibility near the critical point [69]. Therefore, when pressure increases, the fluid density in the current model increases more than that in the color gradient model. Consequently, for a constant mass flow rate at the inlet, the multiphase-phase change model requires more fluid mass, leading to a slower increase in saturation. This indicates that in addition to the phase-change process, the effects of real fluids are also crucial for accurately simulating the displacement of non-phase-change fluids by phase-change fluids. It is worth to notice that the contact angles in this study are all neutral, the variation of the contact angle has not been included in the model. In order to consider the contact angle effect for some real cases such as real rock in porous media, the contact angle adjustment should be considered very careful to coordinate the coupling of contact angle effects of both color gradient and pseudopotential model at the interface of multiphase flow with solid walls.

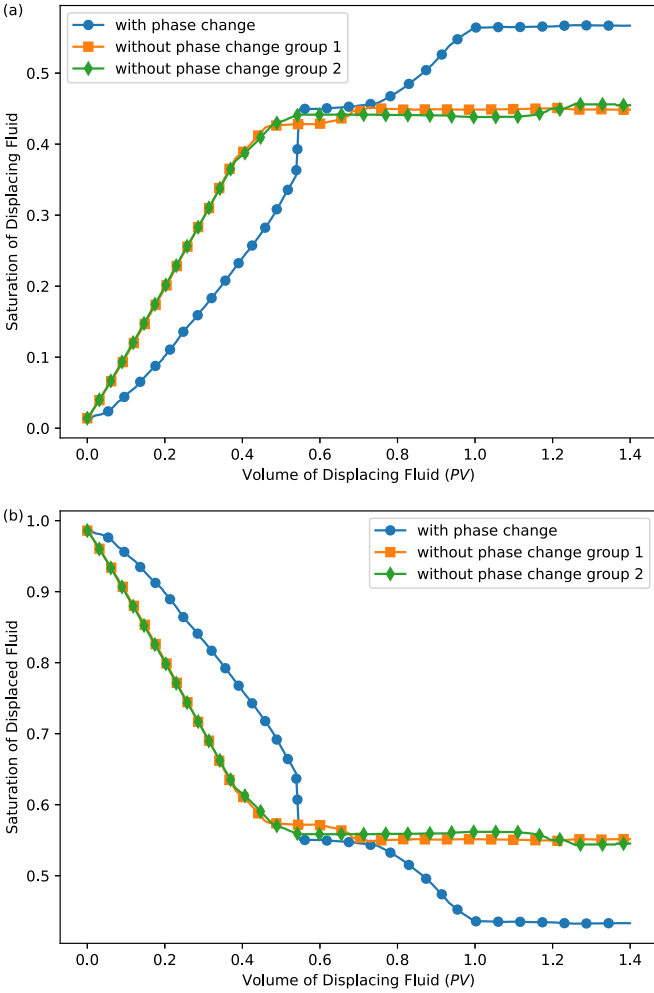


FIG. 16. The saturation of the displacing fluid and the displaced fluid over time. (a) Displacing fluid (phase-change fluid) in the liquid phase; (b) displaced fluid (non-phase-change fluid).

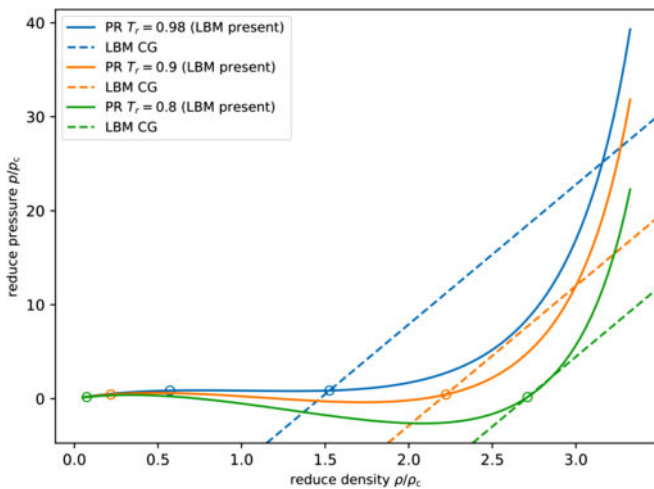


FIG. 17. The EOS of the current model and the conventional color-gradient model. The hollow circles represent saturation states. In the color gradient model, the simulated incompressible flow focuses on relative pressure rather than absolute pressure. For ease of comparison, the EOS of the color gradient model has been shifted accordingly.

V. CONCLUSIONS

In this work, we present a lattice Boltzmann model for immiscible multiphase flow with phase change. By incorporating the pseudopotential model into the color-gradient model to automatically capture the phase change process in immiscible multiphase flow, such as water-oil-gas, where gas and oil may undergo phase change. Assigning different interaction potentials to different color fluids, an immiscible multiphase model that accounts for the phase change process is established. Additionally, we revise the momentum correction term from the literature and verifies the model’s accuracy through standard benchmarks. To the best of our knowledge, this approach represents the first instance of coupling different multiphase LBM models, combining their strength to enhance their capability for complex fluid simulations.

Subsequently, the proposed model is applied to study the phase change effect of multiphase displacement in porous media. Both the phase-change fluid displaced by non-phase-change fluid and the non-phase-change fluid displaced by the phase-change fluid are investigated. The former one shows dramatic difference in capillary numbers and well describes the gas-blockage and displacement path change with phase-change effect. The latter one captures the saturation transition caused by phase-change process and further analyzed the gas compressibility led by the real gas effect. Our results underscore the significant alterations in displacement paths resulting from phase change effects and the compressibility of real gases. Therefore, it is crucial to consider phase change of fluids in applications where such transformations are anticipated.

ACKNOWLEDGMENTS

This work is financially supported by the NSF of the People’s Republic of China (Grants No.12432013 and No. U24B6003) and the Tsinghua University Initiative Scientific Research Program. Our simulations are run on the “Explorer 100” cluster of Tsinghua National Laboratory for Information Science and Technology.

DATA AVAILABILITY

No data were created or analyzed in this study.

APPENDIX A: DERIVATION OF PSEUDOPOTENTIAL SCHEME FOR NON-PHASE-CHANGE FLUID

This Appendix provides the derivation of Eq. (27) and discusses several unsuccessful attempts concerning the pseudopotential scheme for the non-phase-change fluid. This discussion aims to enhance the readers’ understanding of the rationale behind the selection of Eq. (27) and to encourage further development based on this model.

Before formally introducing the derivation of Eq. (27), this paper first walks through several unsuccessful attempts step by step. These failed attempts serve as the foundation for the final form of Eq. (27). Note that the pseudopotential ψ for the phase change fluid is highly dependently on the fluid density

and we assume $\psi_r = \psi_l$ for the bulk phase; therefore, it is natural to define ψ_r based on the bulk density ratio, i.e.,

Scheme 1:

$$\begin{aligned} \psi_r(\rho_{r,\text{eff}}, T) &= \psi(\rho_{r,\text{eff}}, T) \\ &= \sqrt{\frac{2(p_{\text{EOS}}(\rho_{r,\text{eff}}, T) - \rho_{r,\text{eff}}(c_s^r)^2)}{Gc^2}}, \quad (\text{A1}) \\ \rho_{r,\text{eff}} &= \frac{\rho_r}{\gamma_{rl}}. \quad (\text{A2}) \end{aligned}$$

Note that $\rho_{r,\text{eff}} = \rho_b$ at the bulk phase while ψ_r varies smoothly with the density at the interface region. However, since the EOS concerning $\rho_{r,\text{eff}}$ and ρ_b are identical, Scheme 1 cannot prevent the phase change of fluid r , in other words, there exists $\rho_{r,l}$ and $\rho_{r,v}$ which satisfies

$$(c_s^r)^2 \rho_{r,l} + \frac{c^2 G}{2} (\psi_{r,l})^2 = (c_s^r)^2 \rho_{r,v} + \frac{c^2 G}{2} (\psi_{r,v})^2. \quad (\text{A3})$$

As a result, fluid r may phase change under certain condition as Fig. 18(c) demonstrates.

To address the limitations of Scheme 1, the minimum value of $\rho_{r,\text{eff}}$ at the bulk phase should be defined. This minimum value is determined by the liquid saturation density of fluid b , $\rho_{\text{sat}}^{b,l}$ (ρ_{sat}^l for short). Meanwhile, Scheme 1 is employed at the interface region to maintain the smooth variation of ψ_r , i.e.,

Scheme 2:

$$\rho_{r,\text{eff}} = \begin{cases} \frac{\rho_r}{\gamma_{rl}}, & C \leq C' \\ \max\left(\frac{\rho_r}{\gamma_{rl}}, \rho_{\text{sat}}^l\right), & C > C' \end{cases} \quad (\text{A4})$$

where $C = (\rho_r - \rho_b)/(\rho_r + \rho_b)$ is the order parameter distinguishing fluid r and fluid b and C' is the critical value. However, the choice of C' can be challenging. A smaller C' value, such as $C' = 0.99$, can cause discontinuities in ψ at the interface region, which may lead to numerical instabilities—particularly in porous media where complex boundary conditions are present. Figures 19(a)–19(c) illustrate the local phase distribution, interaction potential ψ distribution, and interaction force F^{SC} distribution of a simulation with porous media using Scheme 2. The complex geometry of the porous media results in discontinuities in ψ near the solid walls, leading to large interaction forces F^{SC} and subsequent divergence. On the other hand, a larger C' value $C' = 0.999999$ creates a thicker interface region, which induce partial phase change in fluid r , resulting in divergence.

Therefore, we present Scheme 3 which aims to provide a more continuous transition from the bulk region to the interface region. Since the most crucial problem of ψ is at the r - v interface ($\psi_r = \psi_l$ at the r - l interface), our analysis will focus on the r - v interface. Theoretically, for a diffuse interface, the density profile of the r - v interface is (assuming the interface width is 1, hereafter) [70,71],

$$\rho_b(x) = \frac{\rho_v}{2} + \frac{\rho_v}{2} \tanh(-x) = \frac{\rho_v}{2} - \frac{\rho_v}{2} \tanh(x), \quad (\text{A5})$$

$$\rho_r(x) = \frac{\rho_r}{2} + \frac{\rho_r}{2} \tanh(x), \quad (\text{A6})$$

$$\rho(x) = \rho_b(x) + \rho_r(x) = \frac{\rho_r + \rho_v}{2} + \frac{\rho_r - \rho_v}{2} \tanh(x). \quad (\text{A7})$$

while the density profile of the l - v interface is

$$\rho(x) = \rho_b(x) = \frac{\rho_l + \rho_v}{2} + \frac{\rho_l - \rho_v}{2} \tanh(x). \quad (\text{A8})$$

Here ρ_l and ρ_v denotes the bulk density of liquid phase and vapor phase of fluid b .

Our intention is to mimic the density profile of the l - v interface at the r - v interface, i.e.,

$$\rho(x) = \rho_b(x) + \rho_{r,\text{eff}}(x) = \frac{\rho_l + \rho_v}{2} + \frac{\rho_l - \rho_v}{2} \tanh(x), \quad (\text{A9})$$

$$\rho_{r,\text{eff}}(x) = \frac{\rho_l}{2} + \frac{\rho_l}{2} \tanh(x) = \frac{\rho_r(x)}{\gamma_{rl}}. \quad (\text{A10})$$

However, in the bulk region, following the idea of Scheme 2, $\min(\rho_{r,\text{eff}}) = \rho_{\text{sat}}^l$. Therefore, a function $f(x)$ is required such that $f(x)\rho_{\text{sat}}^l \rightarrow \frac{\rho_l}{2} + \frac{\rho_l}{2} \tanh(x)$ when $C \rightarrow 1$. Since the bulk density $\rho_l = \rho_{\text{sat}}^l$ at the equilibrium, $f(x) \rightarrow 1/2(1 + \tanh(x))$ when $C \rightarrow 1$.

Note that $C = (\rho_r - \rho_b)/(\rho_r + \rho_b)$ is also continuous at the interface region while serving as the order parameter between fluid r and fluid b , whose profile is

$$\begin{aligned} C(x) &= \frac{\rho_r(x) - \rho_v(x)}{\rho_r(x) + \rho_v(x)} \\ &= \frac{(\rho_r - \rho_v) + (\rho_r + \rho_v)\tanh(x)}{(\rho_r + \rho_v) + (\rho_r - \rho_v)\tanh(x)} \\ &= \frac{\rho_r(1 + \tanh(x)) - \rho_v(1 - \tanh(x))}{\rho_r(1 + \tanh(x)) + \rho_v(1 - \tanh(x))}. \end{aligned} \quad (\text{A11})$$

According to

$$1 + \tanh(x) = \frac{2e^{2x}}{e^{2x} + 1}, \quad 1 - \tanh(x) = \frac{2}{e^{2x} + 1}, \quad \gamma_{rv} = \frac{\rho_r}{\rho_v}, \quad (\text{A12})$$

it can be obtained that

$$C(x) = \frac{\rho_r e^{2x} - \rho_v}{\rho_r e^{2x} + \rho_v} = \frac{\gamma_{rv} e^{2x} - 1}{\gamma_{rv} e^{2x} + 1}. \quad (\text{A13})$$

Therefore, we can construct $f(x)$ as

$$\begin{aligned} f(x) &= \frac{\rho_r}{2\rho_v}(C - 1) + 1 \\ &= \frac{\rho_r}{2\rho_v} \left(-\frac{2\rho_v}{\rho_r e^{2x} + \rho_v} \right) + 1 \\ &= 1 - \frac{\rho_r}{\rho_r e^{2x} + \rho_v} \\ &= 1 - \frac{1}{e^{2x} + \frac{\rho_v}{\rho_r}} \rightarrow 1 - \frac{1}{e^{2x} + 1} \\ &= \frac{1}{2}(1 + \tanh(x)) \quad C \rightarrow 1. \end{aligned} \quad (\text{A14})$$

And the Scheme 3 is

$$\rho_{r,\text{eff}} = \max\left(\frac{\rho_r}{\gamma_{rl}}, \rho_{l,\text{sat}} \left(\frac{\gamma_{rv}(C - 1) + 2}{2} \right)\right). \quad (\text{A15})$$

It can be observed in Figs. 18 and 19 that Scheme 3 prevents the phase change of fluid r and avoids the divergence induced by the discontinuity of ψ .

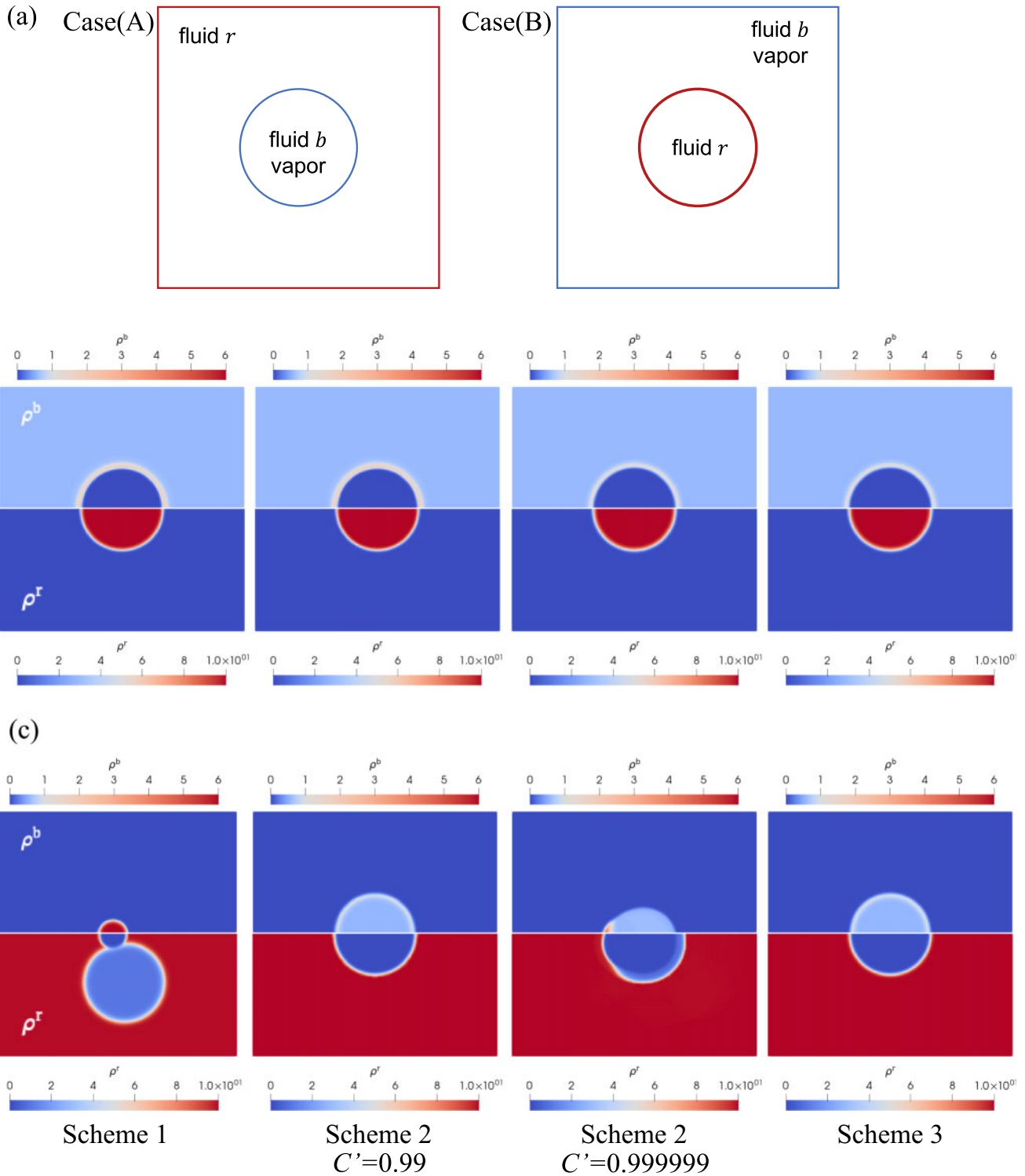


FIG. 18. Simulation results of stationary droplets (bubbles) with r - v interface using different schemes. (a) Case setups: Case A, initially, a circular droplet of fluid r is located at the center; Case B, initially, a circular bubble of fluid v is located at the center. (b) Simulation results for Case A using different schemes, with the top half showing the distribution of ρ_b and the bottom half showing the distribution of ρ_r . (c) Simulation results for Case B using different schemes, with the top half showing the distribution of ρ_b and the bottom half showing the distribution of ρ_r . All cases use a mesh size of 200×200 , with $\sigma_{rv} = 0.2$, $\sigma_{rl} = 0.1$, $\sigma_{tv} = 0.099$, and $\nu = 0.4$. Periodic boundary conditions are applied. In Case B, the simulation diverges after 100 000 steps adopting Scheme 2 with $C' = 0.999999$; the results shown are after 95 000 steps. All other results are from simulations that reached a steady state.

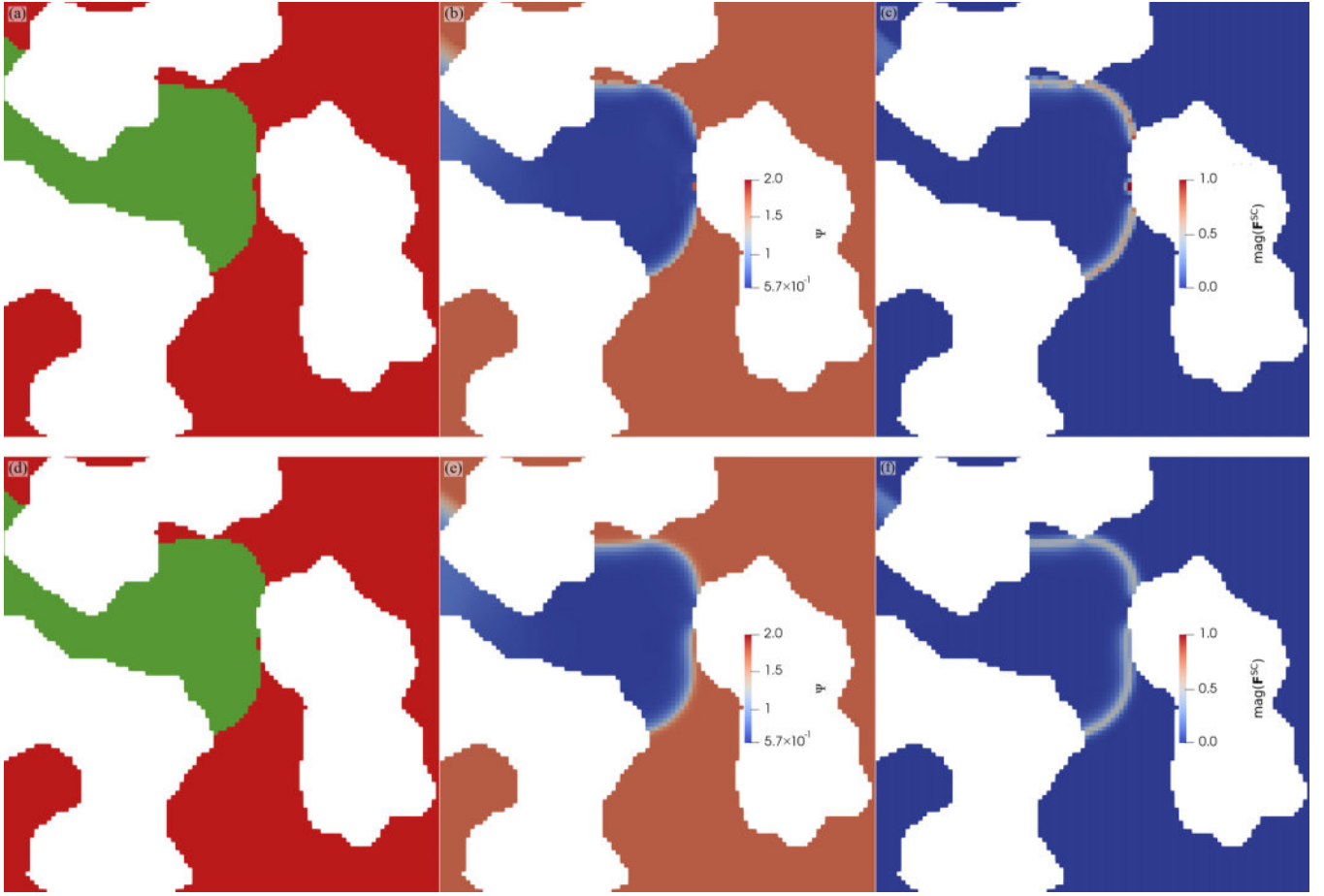


FIG. 19. Local view of simulation results of Scheme 2 and Scheme 3 in porous media. [(a)–(c)] Results from Scheme 2 and [(d)–(f)] from Scheme 3. [(a) and (d)] Phase distribution: Green indicates the vapor phase of fluid b , and red indicates fluid r ; [(b) and (e)] show the interaction potential ψ ; [(c) and (f)] magnitude of the interaction force $|\mathbf{F}^{\text{SC}}|$. The results for Scheme 2 are shown just before divergence occurs. [(b) and (c)] Large localized forces $|\mathbf{F}^{\text{SC}}|$ can be observed, caused by discontinuities in ψ near the solid boundaries, leading to divergence in subsequent simulations. In contrast, under the same parameters and time steps, Scheme 3—shown in (d) and (e)—displays smooth transitions in ψ without divergence. Simulation parameters are $\sigma_{rv} = 0.2$, $\sigma_{rl} = 0.1$, $\sigma_{lv} = 0.099$, and $\nu = 0.2$, with $C' = 0.99$ in Scheme 2.

APPENDIX B: PARAMETERS FOR 2D LBM MODEL

Matrix of 2D and the parameters are shown as follows for D2Q9:

$$\mathbf{S} = \text{diag}(S_\rho, S_e, S_\varepsilon, S_j, S_q, S_j, S_q, S_\nu, S_\nu), \quad (\text{B1})$$

where S_ν is related to the viscosity via $\frac{1}{S_\nu} = \bar{\tau} = \frac{\bar{\nu}}{c_s^2 \delta t} + \frac{1}{2}$.

Meanwhile, the relaxation parameter corresponds to the conserved moments, like density and momentum, should en-

sure $S_\rho = S_j = 0$. Other parameters can be

$$\begin{aligned} S_\rho = S_j = 0, \quad S_\varepsilon = 1.0, \\ \frac{1}{S_e} = \frac{1}{S_\nu} = \tau = \frac{\nu_{\text{eff}}}{c_s^2 \delta t} + \frac{1}{2}, \\ S_q = 1.5. \end{aligned} \quad (\text{B2})$$

- [1] J. J. Sheng *et al.*, Critical review of foamy oil flow, *Transp. Porous Media* **35**, 157 (1999).
- [2] S. Thomas, Enhanced oil recovery—An overview, *Oil Gas Sci. Technol. Rev. IFP* **63**, 9 (2008).
- [3] D. N. Espinoza, S. H. Kim, and J. C. Santamarina, CO₂ geological storage—Geotechnical implications, *KSCE J. Civ. Eng.* **15**, 707 (2011).
- [4] Y. Cai *et al.*, Phase transition and fluid backflow during the non-injection period in the Ordos CCS project, China, *J. Clean. Prod.* **349**, 131493 (2022).
- [5] P. K. Gupta and B. Yadav, VOCs and GHGs intrusion and its impacts on subsurface microbial community, in *Fate and Transport of Subsurface Pollutants* (Springer, Berlin, 2021), Vol. 24, pp. 243–258.
- [6] L. C. Malan *et al.*, A geometric VOF method for interface resolved phase change and conservative thermal energy advection, *J. Comput. Phys.* **426**, 109920 (2021).
- [7] S. Whitaker, Simultaneous heat, mass, and momentum transfer in porous media: A theory of drying, in *Advances in Heat Transfer Volume 13* (Elsevier, Amsterdam, 1977), pp. 119–203.
- [8] P. Zhang and H. W. Jia, Evolution of flow patterns and the associated heat and mass transfer characteristics during flow boiling in mini-/micro-channels, *Chem. Eng. J.* **306**, 978 (2016).
- [9] L. Anumolu and M. F. Trujillo, Gradient augmented level set method for phase change simulations, *J. Comput. Phys.* **353**, 377 (2018).
- [10] F. O. Alpak, B. Riviere, and F. Frank, A phase-field method for the direct simulation of two-phase flows in pore-scale media using a non-equilibrium wetting boundary condition, *Comput. Geosci.* **20**, 881 (2016).
- [11] F.-C. Yang, X.-P. Chen, and P. Yue, Surface roughness effects on contact line motion with small capillary number, *Phys. Fluids* **30**, 012106 (2018).
- [12] T. Kunugi, Brief review of latest direct numerical simulation on pool and film boiling, *Nucl. Eng. Technol.* **44**, 847 (2012).
- [13] A. Markus and G. Hazi, Simulation of evaporation by an extension of the pseudopotential lattice Boltzmann method: A quantitative analysis, *Phys. Rev. E* **83**, 046705 (2011).
- [14] G. Hazi and A. Markus, On the bubble departure diameter and release frequency based on numerical simulation results, *Int. J. Heat Mass Transf.* **52**, 1472 (2009).
- [15] Q. Li *et al.*, Lattice Boltzmann methods for multiphase flow and phase-change heat transfer, *Prog. Energy Combust. Sci.* **52**, 62 (2016).
- [16] A. K. Gunstensen, D. H. Rothman, S. Zaleski, and G. Zanetti, Lattice Boltzmann model of immiscible fluids, *Phys. Rev. A* **43**, 4320 (1991).
- [17] D. H. Rothman and J. M. Keller, Immiscible cellular-automaton fluids, *J. Stat. Phys.* **52**, 1119 (1988).
- [18] X. Shan and H. Chen, Simulation of nonideal gases and liquid-gas phase transitions by the lattice Boltzmann equation, *Phys. Rev. E* **49**, 2941 (1994).
- [19] X. Shan and H. Chen, Lattice Boltzmann model for simulating flows with multiple phases and components, *Phys. Rev. E* **47**, 1815 (1993).
- [20] M. R. Swift, E. Orlandini, W. R. Osborn, and J. M. Yeomans, Lattice Boltzmann simulations of liquid-gas and binary fluid systems, *Phys. Rev. E* **54**, 5041 (1996).
- [21] X. He, X. Shan, and G. D. Doolen, Discrete Boltzmann equation model for nonideal gases, *Phys. Rev. E* **57**, R13 (1998).
- [22] T. Inamuro, T. Ogata, S. Tajima, and N. Konishi, A lattice Boltzmann method for incompressible two-phase flows with large density differences, *J. Comput. Phys.* **198**, 628 (2004).
- [23] H. Huang, M. Sukop, and X. Lu, *Multiphase Lattice Boltzmann Methods: Theory and Application* (Wiley, West Sussex, 2015).
- [24] H. Liu *et al.*, Multiphase lattice Boltzmann simulations for porous media applications, *Comput. Geosci.* **20**, 777 (2015).
- [25] M. Soomro and L. F. Ayala, Unrestricted component count in multiphase lattice Boltzmann: A fugacity-based approach, *Phys. Rev. E* **108**, 035304 (2023).
- [26] Z. Guo, Well-balanced lattice Boltzmann model for two-phase systems, *Phys. Fluids* **33**, 031709 (2021).
- [27] L. Chen *et al.*, A critical review of the pseudopotential multiphase lattice Boltzmann model: Methods and applications, *Int. J. Heat Mass Transfer* **76**, 210 (2014).
- [28] Q. Lou, Z. L. Guo, and B. C. Shi, Effects of force discretization on mass conservation in lattice Boltzmann equation for two-phase flows, *Europhys. Lett.* **99**, 64005 (2012).
- [29] G. Yang and M. Wang, Surface roughness effect on dynamic wettability in imbibition process, *Comput. Fluids* **263**, 105959 (2023).
- [30] S. Leclaire, A. Parmigiani, O. Malaspinas, B. Chopard, and J. Latt, Generalized three-dimensional lattice Boltzmann color-gradient method for immiscible two-phase pore-scale imbibition and drainage in porous media, *Phys. Rev. E* **95**, 033306 (2017).
- [31] T. Akai, B. Bijeljic, and M. J. Blunt, Wetting boundary condition for the color-gradient lattice Boltzmann method: Validation with analytical and experimental data, *Adv. Water Res.* **116**, 56 (2018).
- [32] C. Xie, W. Lei, and M. Wang, Lattice Boltzmann model for three-phase viscoelastic fluid flow, *Phys. Rev. E* **97**, 023312 (2018).
- [33] S. Leclaire *et al.*, Enhanced equilibrium distribution functions for simulating immiscible multiphase flows with variable density ratios in a class of lattice Boltzmann models, *Int. J. Multiphase Flow* **57**, 159 (2013).
- [34] S. Gong and P. Cheng, Lattice Boltzmann simulation of periodic bubble nucleation, growth and departure from a heated surface in pool boiling, *Int. J. Heat Mass Transf.* **64**, 122 (2013).
- [35] S. Gong and P. Cheng, A lattice Boltzmann method for simulation of liquid–vapor phase-change heat transfer, *Int. J. Heat Mass Transf.* **55**, 4923 (2012).
- [36] L. Fei, D. Derome, and J. Carmeliet, Pore-scale study on the effect of heterogeneity on evaporation in porous media, *J. Fluid Mech.* **983**, A6 (2024).
- [37] L. Fei *et al.*, Lattice Boltzmann modelling of isothermal two-component evaporation in porous media, *J. Fluid Mech.* **955**, A18 (2023).
- [38] Q. Li, Y. Yu, and Z. X. Wen, How does boiling occur in lattice Boltzmann simulations? *Phys. Fluids* **32**, 093306 (2020).
- [39] R. Zhang and H. Chen, Lattice Boltzmann method for simulations of liquid-vapor thermal flows, *Phys. Rev. E Stat. Nonlin. Soft Matter Phys.* **67**, 066711 (2003).
- [40] A. L. Kupershtokh, D. A. Medvedev, and D. I. Karpov, On equations of state in a lattice Boltzmann method, *Comput. Math. Appl.* **58**, 965 (2009).

- [41] Q. Li, K. H. Luo, and X. J. Li, Lattice Boltzmann modeling of multiphase flows at large density ratio with an improved pseudopotential model, *Phys. Rev. E* **87**, 053301 (2013).
- [42] Q. Li, K. H. Luo, and X. J. Li, Forcing scheme in pseudopotential lattice Boltzmann model for multiphase flows, *Phys. Rev. E* **86**, 016709 (2012).
- [43] Q. Li *et al.*, Lattice Boltzmann modeling of boiling heat transfer: The boiling curve and the effects of wettability, *Int. J. Heat Mass Transf.* **85**, 787 (2015).
- [44] S. Gong and P. Cheng, Direct numerical simulations of pool boiling curves including heater's thermal responses and the effect of vapor phase's thermal conductivity, *Int. Commun. Heat Mass Transf.* **87**, 61 (2017).
- [45] C. Zhang *et al.*, Lattice Boltzmann mesoscopic modeling of flow boiling heat transfer processes in a microchannel, *Appl. Therm. Eng.* **197**, 117369 (2021).
- [46] S. Leclaire, M. Reggio, and J.-Y. Trépanier, Progress and investigation on lattice Boltzmann modeling of multiple immiscible fluids or components with variable density and viscosity ratios, *J. Comput. Phys.* **246**, 318 (2013).
- [47] C. Xie *et al.*, Self-adaptive preferential flow control using displacing fluid with dispersed polymers in heterogeneous porous media, *J. Fluid Mech.* **906**, A10 (2020).
- [48] J. Latt *et al.*, Palabos: Parallel lattice Boltzmann solver, *Comput. Math. Appl.* **81**, 334 (2021).
- [49] Z. Guo, C. Zheng, and B. Shi, Discrete lattice effects on the forcing term in the lattice Boltzmann method, *Phys. Rev. E* **65**, 046308 (2002).
- [50] T. Krüger *et al.*, *The Lattice Boltzmann Method: Principles and Practice* (Springer, Cham, 2017).
- [51] D. D'Humieres *et al.*, Multiple-relaxation-time lattice Boltzmann models in three dimensions, *Philos. Trans. A Math. Phys. Eng. Sci.* **360**, 437 (2002).
- [52] D. d'Humieres, Generalized lattice Boltzmann equations, in *Rarefied Gas Dynamics: Theory and Simulations* (AIAA, Reston, VA, 1992).
- [53] L. S. Luo *et al.*, Numerics of the lattice Boltzmann method: Effects of collision models on the lattice Boltzmann simulations, *Phys. Rev. E* **83**, 056710 (2011).
- [54] T. Reis and T. N. Phillips, Lattice Boltzmann model for simulating immiscible two-phase flows, *J. Phys. A Math. Theor.* **40**, 4033 (2007).
- [55] M. Latva-Kokko and D. H. Rothman, Diffusion properties of gradient-based lattice Boltzmann models of immiscible fluids, *Phys. Rev. E* **71**, 056702 (2005).
- [56] X. Shan, Pressure tensor calculation in a class of nonideal gas lattice Boltzmann models, *Phys. Rev. E* **77**, 066702 (2008).
- [57] P. Yuan and L. Schaefer, Equations of state in a lattice Boltzmann model, *Phys. Fluids*. **18**, 042101 (2006).
- [58] Q. Li *et al.*, Enhancement of boiling heat transfer using hydrophilic-hydrophobic mixed surfaces: A lattice Boltzmann study, *Appl. Therm. Eng.* **132**, 490 (2018).
- [59] H. X. Li *et al.*, Effect of surface wettability and gas/liquid velocity ratio on microscale two-phase flow patterns, in *Proceedings of the ASME 5th International Conference on Micro/Nanoscale Heat and Mass Transfer* (ASME, New York, 2016), Vol 2.
- [60] S. Gong and P. Cheng, Lattice Boltzmann simulations for surface wettability effects in saturated pool boiling heat transfer, *Int. J. Heat Mass Transf.* **85**, 635 (2015).
- [61] X. Ma, P. Cheng, and X. Quan, Simulations of saturated boiling heat transfer on bio-inspired two-phase heat sinks by a phase-change lattice Boltzmann method, *Int. J. Heat Mass Transf.* **127**, 1013 (2018).
- [62] X. Ma and P. Cheng, 3D simulations of pool boiling above smooth horizontal heated surfaces by a phase-change lattice Boltzmann method, *Int. J. Heat Mass Transf.* **131**, 1095 (2019).
- [63] L. N. Dong, S. Gong, and P. Cheng, Direct numerical simulations of film boiling heat transfer by a phase-change lattice Boltzmann method, *Int. Commun. Heat Mass Transf.* **91**, 109 (2018).
- [64] Q. Li, P. Zhou, and H. J. Yan, Improved thermal lattice Boltzmann model for simulation of liquid-vapor phase change, *Phys. Rev. E* **96**, 063303 (2017).
- [65] Y. Yu *et al.*, A versatile lattice Boltzmann model for immiscible ternary fluid flows, *Phys. Fluids*. **31**, 012108 (2019).
- [66] M. J. Blunt, *Multiphase Flow in Permeable Media a Pore-scale* (Cambridge University Press, Cambridge, UK, 2017).
- [67] S. Zeppieri, J. Rodríguez, and A. L. López de Ramos, Interfacial tension of alkane + water systems, *J. Chem. Eng. Data*. **46**, 1086 (2001).
- [68] Q. Zou and X. He, On pressure and velocity boundary conditions for the lattice Boltzmann BGK model, *Phys. Fluids*. **9**, 1591 (1997).
- [69] M. Tabatabaian and R. Rajput, *Advanced Thermodynamics: Fundamentals, Mathematics, Applications* (De Gruyter, Berlin, 2017).
- [70] H. B. Callen, *Thermodynamics and an Introduction to Thermostatistics* (Wiley, New York, 1985).
- [71] J. S. Rowlinson and B. Widom, *Molecular Theory of Capillarity* (Clarendon, Oxford, 1989).